A 25-micrometer Single-Photon-Sensitive Kinetic Inductance Detector

Day, Peter K.; Cothard, Nicholas F.; Albert, Christopher; Foote, Logan; Kane, Elijah; Eom, Byeong H.; Van Berkel, Sven; Dabironezare, Shahab; Baselmans, Jochem J.A.; More Authors

Important note
To cite this publication, please use the final published version (if applicable).
Please check the document version above.

A 25-micrometer Single-Photon-Sensitive Kinetic Inductance Detector

Peter K. Day[1,*] Nicholas F. Cothard[2] Christopher Albert[3] Logan Foote[3] Elijah Kane[3] Byeong H. Eom[1]
Ritoban Basu Thakur[1] Reinier M. J. Janssen[1] Andrew Beyer[1] Pierre M. Echternach[1] Sven van Berkel[1]
Steven Hailey-Dunsheath[3] Thomas R. Stevenson[2] Shahab Dabironezare[4,5] Jochem J. A. Baselmans[4,5]
Jason Glenn[2] C. Matt Bradford[1,3] and Henry G. Leduc[1]

[1]*Jet Propulsion Laboratory*, California Institute of Technology, 4800 Oak Grove Drive,
Pasadena, California 91109, USA
[2]*NASA Goddard Space Flight Center*, 8800 Greenbelt Road, Greenbelt, Maryland 20771, USA
[3]*California Institute of Technology*, 1200 California Boulevard, Pasadena, California 91125, USA
[4]*SRON Netherlands Institute for Space Research*, Niels Bohrweg 4, Leiden, 2333 CA, The Netherlands
[5]*Department of Microelectronics, Delft University of Technology, Mekelweg 4,
Delft 2628 CD, The Netherlands*

We report measurements characterizing the performance of a kinetic inductance detector array designed for a wavelength of 25 microns and very low optical background level suitable for applications such as a far-infrared instrument on a cryogenically cooled space telescope. In a pulse-counting mode of operation at low optical flux, the detectors can resolve individual 25-micron photons. In an integrating mode, the detectors remain photon noise limited over more than 6 orders of magnitude in absorbed power from 70 zW to 200 fW, with a limiting noise equivalent power of 4.6×10^{-20} W Hz^{-1} at 1 Hz. In addition, the detectors are highly stable with flat power spectra under optical load down to 1 mHz. Operational parameters of the detector are determined including the efficiency of conversion of the incident optical power into quasiparticles in the aluminum absorbing element and the quasiparticle self-recombination constant.

I. INTRODUCTION

The thermal infrared through millimeter-wave band (approximately 5–2000 μm) has great promise for breakthrough measurements in fields ranging from exoplanet spectroscopy, planet formation, galaxy evolution, and cosmology. Relative to the optical bands, the thermal IR (approximately 5–25 μm) offers relaxed contrast between planets and their host stars and carries spectral features of many biogenic gases. This band is being developed for transit spectroscopy with the James Webb Space Telescope [1,2], and future concepts are targeting direct exoplanet spectroscopy via interferometric nulling from space [3]. In the far IR (approximately 25–300 μm), massive gains are possible for general astrophysics, including planet formation and galaxy evolution, with a cryogenic space-borne

telescope [4,5]. In the submillimeter and millimeter (approximately 300–2000 μm), wide-field imaging spectroscopy creating tomographic maps of the Universe provides unique constraints at the intersection of cosmology [6] and galaxy evolution in the first billion years after the big bang [7,8].

Realizing these opportunities, however, requires high-performance detector arrays which are not available from commercial providers. Exoplanet transit work requires excellent stability (approximately 10 ppm or better) over many hour timescales [9] to accurately difference the planet from the star. Far-IR astrophysics and millimeter-wave cosmology require exquisite per-pixel sensitivity [noise equivalent power (NEP) $\lesssim 10^{-19}$ W Hz$^{-1/2}$] to match the natural backgrounds of a cryogenic space-borne platform, combined with high dynamic range (approximately 10^5) to accommodate the diversity of sources. All applications require many-kilopixel array formats, necessitating efficient multiplexing.

Superconducting pair-breaking detectors, including kinetic inductance detectors (KIDs) [10,11], superconducting tunnel junction (STJ) detectors [12], and quantum capacitance detectors (QCDs) [13], are a powerful emerging approach for this next generation of observatories and

*Contact author: Peter.K.Day@jpl.nasa.com

instruments. These devices operate by sensing changes in the Cooper pair density through the quasiparticle population produced by absorbed photons. Owing to the small value of superconducting gap energy, typically hundreds of µeV, these detectors can operate through the far-IR and much of the millimeter-wave bands; aluminum, for example, has a pair-breaking energy threshold corresponding to 90 GHz. In the far infrared through millimeter, the devices typically work as total power detectors: Fluctuations in the absorbed power create corresponding fluctuations in the quasiparticle density. Recent efforts have yielded both KIDs and QCDs with noise equivalent power better than 10^{-19} W Hz$^{-1/2}$ [13–16], meeting the requirements for space-borne moderate-resolution spectroscopy in the 200–300 µm regime. At shorter near-IR through visible wavelengths, each absorbed photon breaks enough Cooper pairs to produce a measurable pulse response, so the detector can operate in a photon-counting mode where the detected pulse amplitudes indicate the photon energies, and the arrival times can be determined [17]. KIDs, in particular, have emerged as versatile detectors, given successes in ground-based and balloon-borne instrumentation in both the far IR to millimeter [18–24] and the optical [25,26], as well as advances in readout electronics [27–30].

Here, we describe a KID demonstration at an intermediate, mid-IR wavelength of 25 µm, which is of prime interest for future space-borne astrophysics experiments. It operates in both integrating and photon-counting modes depending on the optical flux. At low arrival rates, individual 25-micron photons are detected and can be distinguished from other events, such as cosmic rays or background radiation, based on the pulse amplitudes. At higher arrival rates, the detector acts as a shot-noise-limited integrating detector over a dynamic range exceeding 6 orders of magnitude in optical power. In that mode, the detector is stable on the timescale of hours, allowing for deep integration to measure small fractional changes in optical flux. Section II provides a brief description of the detector, Sec. III presents the principal results, and Sec. IV outlines the methods used. Sections V and VI provide context and summarize.

II. DEVICE

KIDs operate by sensing the effect of optically excited quasiparticles on the complex conductivity of the inductive element of a superconducting microresonator. At far-IR wavelengths, efficient optical coupling has been achieved using either wire grid absorbers (e.g., Ref. [31]) or various antenna structures (e.g., Ref. [11]). Both of these techniques are compatible with low inductor volumes needed to enhance the detector sensitivity, particularly when used in concert with a microlens array or feedhorn array. Here, we present a KID design for 25 microns, around the short-wavelength end of the far-infrared band, where antenna coupling becomes inefficient due to conductor loss and feedhorn manufacture is not practical due to surface

roughness requirements. These considerations drive us to a microlens-absorber coupled approach. While many such devices for submillimeter to optical frequencies have used high-normal-state-resistivity superconductors which allow straightforward resistive absorption, our device builds on our earlier work showing that an absorber incorporating resonant structures [32,33] can have high efficiency in the far IR even when using a low-resistivity aluminum film, now considered the material of choice for most KID applications. Our array builds on that presented in Ref. [32] but incorporates both further reduced volume and improved quasiparticle lifetime. These factors combine to create a detector that is photon-shot-noise limited under the attowatt level optical loading predicted for space-borne far-infrared spectroscopy.

The detector array consists of 44 KIDs arranged on a hexagonal lattice with a pitch of 900 microns. The layout of a pixel is shown in Fig. 1. It consists of a 70-micron-diameter aluminum meandered inductive section in parallel with a niobium interdigitated capacitor (IDC) forming a resonator. The resonance frequencies are distributed log uniformly in the range of 570–1120 MHz. Coupling quality factors Q_c are distributed in the range of 2×10^4–10^5, and the unilluminated internal quality factors are $Q_i \approx 10^6$. Details on the array uniformity are described in Appendix D. The array is fabricated on a high-resistivity silicon wafer with a similar process to that described in Ref. [15], except that the aluminum film thickness is 40 nm and the linewidth of the inductor is reduced to 100 nm in order to minimize its volume. The meander is similar to the one described in Ref. [32] except for narrower linewidth and is made up of the repeated unit cell shown in Fig. 1(e). The pattern, which acts as a frequency selective surface, is designed to resonantly absorb incident light in a band around 25 microns in both polarizations. The optically generated quasiparticles are confined to the aluminum because of the higher niobium gap parameter. We estimate an aluminum volume of 11 µm^3, taking into account that, as fabricated, the lines are slightly wider than designed. Light is focused on the aluminum absorbers using an antireflection-coated silicon lenslet array that is glued to the back side of the detector wafer using a submicron thickness epoxy layer, as described in Ref. [34]. Eight of the pixels are left without lenses.

III. RESULTS

The measurements are conducted using a standard homodyne circuit to probe the complex transmission coefficient S_{21} of a particular resonator. The microwave probe power is set to be approximately 10 fW, roughly 3 dB less than the bifurcation power of the resonators, which is the power at which the resonance curves become hysteretic [35] due to the nonlinear response of the kinetic inductance. The array is kept at a temperature of 150 mK for most of the measurements. Characterization of the detectors at other bath temperatures is described in Appendix C.
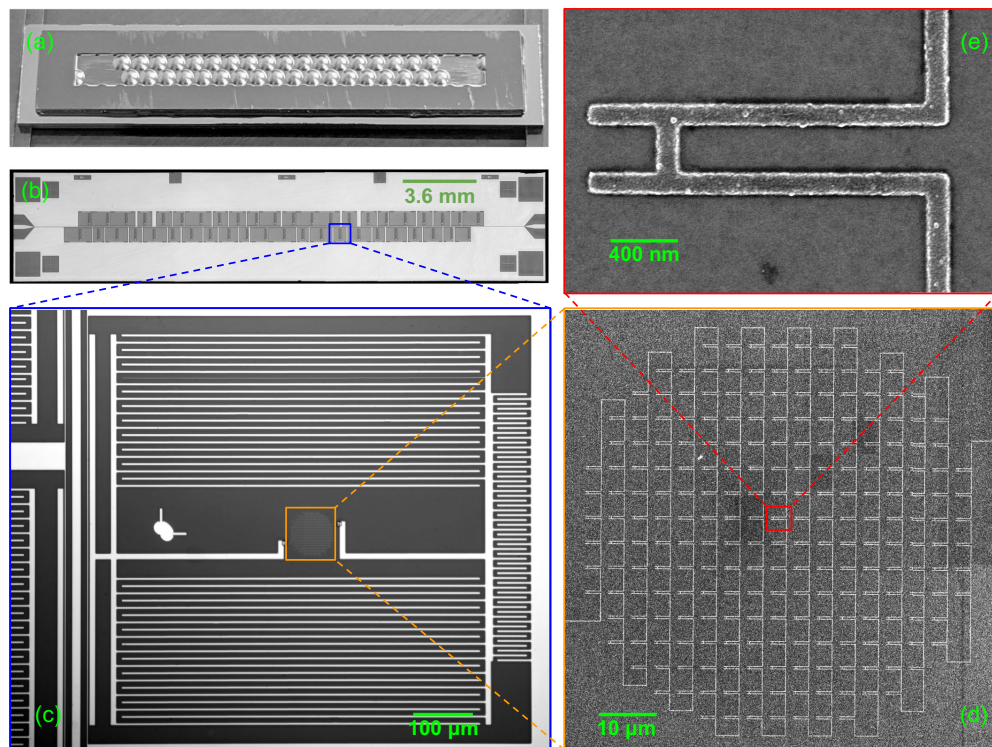
FIG. 1. Photographs and scanning electron microscope (SEM) image of the KID array and components. (a) Photograph of antireflection-coated microlens array. (b) Stitched microscope photographs of the 44-element kinetic inductance detector array. (c) A single KID comprised of a pair of niobium IDCs (upper and lower) surrounding the 70-micron-diameter aluminum absorber (center). The detector is capacitively coupled to a niobium feedline (left) and ground plane (right). (d) SEM image of the meandered aluminum resonant absorber. (e) SEM image of the periodically patterned "hairpin" geometry resonant structure, showing 100 nm linewidth aluminum trace width. The resonant absorber is discussed further in Appendix B.

Changes in $S21$ are converted to changes in the fractional frequency shift $\delta x = \delta f_r / f_r(0)$, where $f_r(0)$ is the average resonance frequency without optical illumination and $\delta f_r = f_r(0) - f_r$ is the resonance frequency perturbation. The detectors are exposed to optical power from a cryogenic blackbody source through a 200-micron-diameter aperture and a set of metal mesh filters that in combination produce a roughly 20% wide passband centered near $\nu = 12\,\text{THz}$ ($\lambda = 25\,\mu\text{m}$), as described in Sec. IV A.

A. Single-photon detection

The filter passband is in the Wien tail of the blackbody spectrum for $T_{BB} \sim 30\,\text{K}$, and only a few photons per second are expected at the detector. Examples of measured time streams are shown in Fig. 2 (left) for different blackbody temperatures. With the blackbody at 3 K, pulse events are rare. With increasing temperature, high signal to noise pulses are observed with increasing rate and eventually become overlapping. Much larger pulses are also observed with a frequency of about 0.2/s and are attributed to either cosmic ray events or background radioactivity and are excluded from our analyses. Using a causal optimal

filter (OF), aligning and coadding many pulses of similar amplitude produces a pulse template that is well represented by an exponential decay with a time constant of 1 ms; see Fig. 2 (right) and Sec. IV D. The decay time is found to be independent of the pulse height for a particular bath temperature.

A pulse tagging algorithm is used to select photonlike pulses with a threshold criteria as n times the standard deviation of the baseline noise. The pulse template then enables extracting the amplitude of each pulse with OF, producing the amplitude histograms shown in Fig. 3, where results are displayed for three threshold values. The histograms show clear Gaussian-shaped peaks with mean $\delta x = 1.54 \times 10^{-6}$ which we identify as photons from the blackbody that pass through the filters. The excess counts at lower amplitudes include both noise-induced false counts and lower-amplitude background photons. The "3σ" cut effectively rejects all noise spikes and selects the photon pulses; see Sec. IV D for details.

The resolving power in energy is defined as $\mathcal{R} = \langle E \rangle / \Delta E_{\text{FWHM}}$. The measured $\mathcal{R}$ necessarily includes all sources of energy broadening. The two broadening
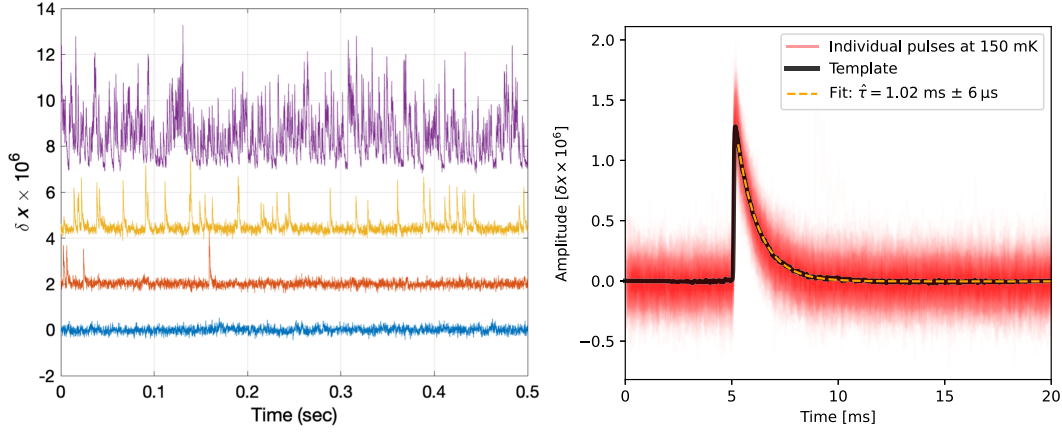
FIG. 2. Left: time streams with the blackbody at (from bottom to top) $T_{BB} = 3$, 30, 35, and 42 K. The data are offset along the y axis for clarity. Right: 548 stacked single-photon pulses (red) at $T_{BB} = 30$ K and 50 kHz sample rate. Alignment is achieved with causal optimal filtering. A single-photon template is obtained via averaging (black) and has a time constant ≈ 1 ms; see fit (orange).

mechanisms in any pulse-detecting instrument are the optical bandpass filter (including the wavelength-dependent response of the absorber) and the energy resolution of the detector itself. The first is determined with Fourier transform spectrometer (FTS) measurements of the filter stack transmission $F(\nu)$ and absorber efficiency $\mathcal{A}_{abs}(\nu)$ independently, as described in Sec. IV A and Appendix B. The detector resolution includes a readout-related contribution set by the detector noise floor integrated through the optimal filter and is approximately given by $\delta E_{rms} \sim NEP\sqrt{\tau}$, where τ is the pulse decay timescale [36].
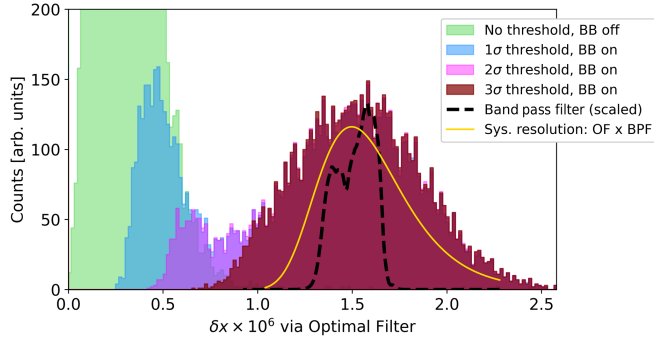

FIG. 3. OF pulse amplitude histograms. The (black) dashed line indicates the net bandpass filter (BPF), i.e., the passband of the metal mesh filters multiplied by the absorber's frequency dependence determined from FTS measurements. The OF energy resolution convolved with the BPF gives the system resolution (yellow). We run OF on randomly sampled noise data with the blackbody "off," without any threshold for pulse selection, and histogram them (green). This is compared with the blackbody "on" at 30 K and varying pulse-selection thresholds as effective 1, 2, and 3σ distances from the noise distribution (blue, magenta, and maroon, respectively). Thus, a clean sample of photonlike pulses is created as the threshold is progressively increased. We particularly note that the system resolution is sufficiently high for Fano-limited single-photon measurements.

Our estimate of the convolution of these two contributors to $\mathcal{R}$ is shown with the thin yellow curve in Fig. 4. We compute an effective resolving power of 2.92; compared to this, the data have an $\mathcal{R} = 1.89$.

Our pair-breaking detector is also subject to statistical variation in the finite number of quasiparticles generated and their timescales for recombination. This Fano limit is given by

$$\mathcal{R}_{FANO} = \frac{1}{2\sqrt{2\log 2}} \sqrt{\frac{\eta_{pb} E_\gamma}{\Delta F}} \approx 8, \tag{1}$$

where the value of 8 is what would be expected with a Fano factor $F \simeq 0.2$ [37] and the pair breaking efficiency $\eta_{pb} = 0.3$ estimated below. This perfect Fano limit should, thus, not limit the $\mathcal{R}$ in our system. The fact that the measured resolving power ($\mathcal{R}_{meas} \sim 1.9$) is lower than the expected value, combined with the relatively low pair-breaking efficiency, suggests that energetic phonon loss [38] is a contributing element to the response of the detector. This is
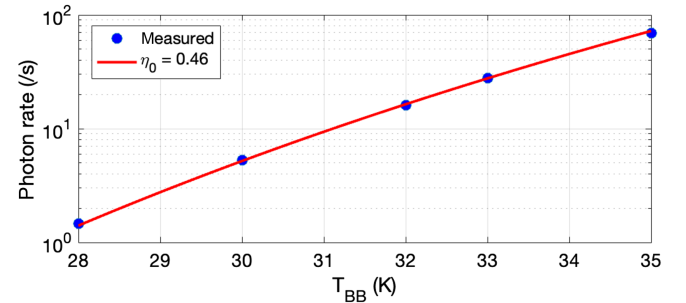

FIG. 4. Measured and expected photon event rates versus blackbody temperature. The measured rate (blue dots) is determined by the methods in Sec. IV D. The red line represents the expected rate computed via Eq. (2), where the efficiency factor of $\eta_o = 0.46$ is chosen to fit the data, suggesting an unquantified system optical efficiency of this value.

not surprising, as the photon energy is similar to the Debye energy, so the phonon-controlled phase of the energy cascade process is similar to that which occurs in detectors for visible and higher-energy photons where energetic phonon loss clearly occurs [39–41].

The measured photon arrival rate Γ_γ for blackbody with temperature T is determined from the area under the Gaussian fit to the pulse amplitude histogram (Fig. 3) in order to exclude noise-induced false counts and low-energy background events. $\Gamma_\gamma(T)$ is shown in Fig. 4 for blackbody temperatures low enough that single photons are observed without significant pileup. The measured rates are compared to the integrated blackbody spectral photon radiance $B(\nu, T)/h\nu$, multiplied by $F(\nu)\mathcal{A}_{\mathrm{abs}}(\nu)$, and constant efficiencies related to the optical system:

$$\Gamma_\gamma(T) = \eta_o \epsilon A\Omega \int \frac{B(\nu, T)}{h\nu} F(\nu)\mathcal{A}_{\mathrm{abs}}(\nu) d\nu, \qquad (2)$$

where A is the microlens area, based on the measured 870 μm diameter, Ω is the solid angle subtended by the 200 μm diameter aperture, and ϵ is the effective emissivity of the blackbody including a small reduction in coupling to the aperture due to diffraction [42]. The parameter η_o accumulates the efficiency with which the microlens couples incident power onto the absorber along with unquantified efficiencies in the system such as an aperture thickness effect. We find that $\eta_o = 0.46$ matches the data. Much of this loss is likely to be due to a deviation in the fabricated lens profile from the design around the edges of the lens. A diffraction calculation using the measured microlens profile suggests a spill-over efficiency of 0.70, compared to 0.94 for the designed profile. The fabricated profile also results in a more tightly focused optical spot on the absorber than intended, which reduces the coupling relative to the infinite array behavior, as the spot size becomes comparable to the size of the unit cell of the absorber pattern. Importing the field distribution from the diffraction calculation into a full-wave EM simulator, we estimate a coupling efficiency of 0.87 compared to optimal defocusing. Further losses of a few percent are expected from the antireflection layer on the lenses and from absorption in the epoxy bond between the detector and microlens array wafers.

B. Quasiparticle conversion efficiency from pulse height

Photon absorption in a superconducting film initiates a phonon-mediated cascade process whereby the energy of the initial photoelectron is transferred to a population of quasiparticles near the gap energy with efficiency $\eta_{\mathrm{pb}} = \Delta_0 N_{\mathrm{qp}}/h\nu$, where $h\nu$ is the absorbed photon energy, N_{qp} is the number of gap edge quasiparticles produced, and Δ_0 is the superconducting gap energy. The remaining energy is lost to phonons. In a thick superconducting film, these phonons have energy $\Omega < 2\Delta_0$ so that they are unable

to break Cooper pairs. In this case, a calculation has found $\eta_{\mathrm{pb}} \approx 0.6$ for aluminum [43]. A similar efficiency has been found for thin films at low photon energies (e.g., 0.85 THz) where only a few quasiparticles are created per photon, based on comparing photon noise with thermal generation-recombination noise [44]. On the other hand, at optical and higher photon energies, energy loss due to escape of $\Omega > 2\Delta_0$ phonons into a solid substrate has been found to be a major limitation on the energy resolution of thin film KID and STJ detectors, as the loss of these energetic phonons increases the statistical fluctuation in the detected energy. For example, our measurement of 1.55 μm (193 THz) photon pulses in our aluminum KIDs suggests a pair-breaking efficiency of 0.13 at these near-IR energies [45].

The efficiency for quasiparticle production by photons with average frequency $\langle\nu\rangle = 12.1$ THz in the 40 nm aluminum film of our detector can be estimated from the average measured pulse height. Using the value of $\delta x/\delta N_{\mathrm{qp}}$ determined in Appendix A,

$$\eta_{\mathrm{pb}} = \frac{\Delta_0}{h\langle\nu\rangle} \frac{\langle\delta x\rangle}{(\delta x/\delta N_{\mathrm{qp}})} = 0.32. \qquad (3)$$

This value agrees well with the value found from the measured noise spectra described below. It is unsurprisingly intermediate between the low-energy limit of approximately 0.6 and the much lower values at optical and near-IR energies. It also agrees with a theoretical treatment of the energy dependence of the pair-breaking efficiency [41,46].

C. Photon-shot-noise-limited sensitivity

The upper left in Fig. 5 shows the fractional frequency noise power spectral densities (PSDs) for a range of optical powers. The noise spectra are well characterized by a low-frequency white component and a roll-off, which contains information on the decay time of the quasiparticles, τ_{qp}. The noise floor at frequencies beyond the roll-off is consistent with the noise of the cryogenic amplifier. At lower optical powers, a low-frequency component is also present that scales approximately as $f^{-1/4}$ in the range shown, indicative of two-level system (TLS) noise. Fits to the noise spectra are overlaid with black dashed lines. The best fit τ_{qp} values are plotted in the upper right in Fig. 5 against the measured fractional frequency optical responsivities for each optical power. The responsivity measurement method is described in Sec. IV C. τ_{qp} and the responsivity scale linearly with each other, as illustrated with the best fit line.

The lower left in Fig. 5 shows the NEP as a function of audio frequency for a range of optical powers. The low-frequency stability of the detector results in stable NEP performance over a wide range of audio frequencies for all optical powers. The lower right in Fig. 5 shows the NEP
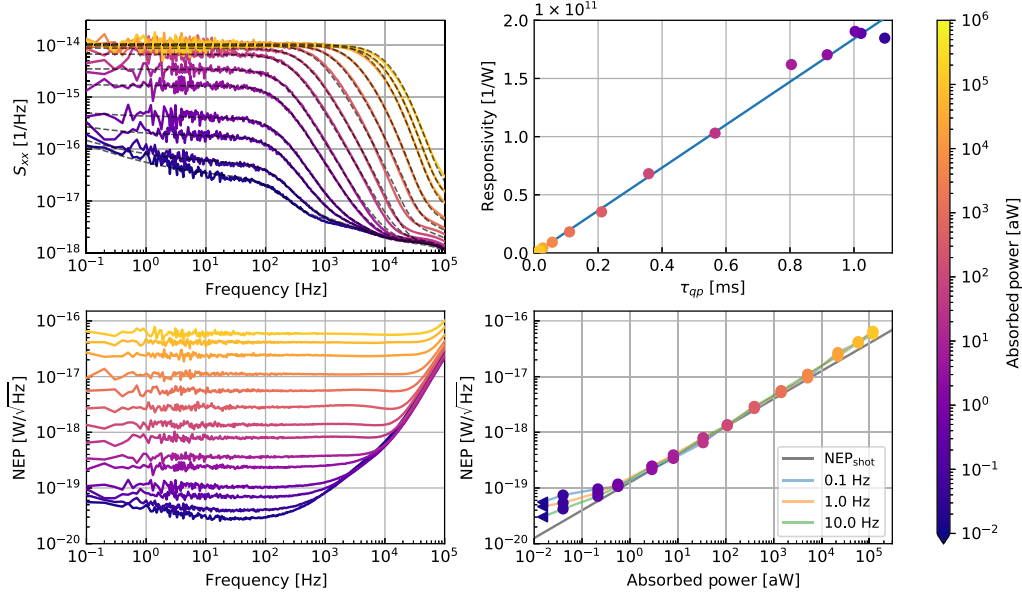
FIG. 5. Detector noise, time constants, and sensitivity as a function of absorbed optical power, which includes the optical efficiency factor of 0.46 determined from the photon count rate in Sec. III A. Upper left: fractional frequency noise spectra show for multiple absorbed powers. Black dashed lines show noise spectra fits incorporating a white noise component, the quasiparticle lifetime, the resonator ringdown time, and a TLS component (significant for only the lowest absorbed powers). Upper right: the measured responsivity as a function of the quasiparticle lifetime extracted from the fractional frequency noise spectra fits, including a linear fit overplotted. Lower: NEP as a function of audio frequency (lower left) and absorbed power (right). Data points with the triangle symbol illustrate measurements with the blackbody infrared source turned off where the true absorbed power of these data points is many orders of magnitude lower. The NEP is shot-noise limited over nearly 6 orders of magnitude of absorbed power.

at 0.1, 1, and 10 Hz as a function of absorbed power. The absorbed power calculation includes the optical efficiency determined from the single-photon arrival rates described in Sec. III A, $\eta_o = 0.46$. When this efficiency is included, the NEP data fall on the theoretical photon-shot-noise curve given by $\text{NEP}_{\text{shot}} = \sqrt{2h\nu P_{\text{abs}}}$ over 6 orders of magnitude of absorbed power. At the lowest absorbed power, where the detector can sense single-photon events, we find a limiting NEP of 4.6×10^{-20} W/$\sqrt{\text{Hz}}$ at 1 Hz for an integrating readout. The NEP in the photon-counting regime is ultimately limited by the dark count rate.

The increase in the white component of the fractional frequency PSDs with power at low optical power and the saturation at high power has been observed in previous studies of MKIDs and has been associated with the saturation of τ_{qp} [47]. As quasiparticle recombination is a pairwise process, the lifetime decreases with the quasiparticle density $n_{\text{qp}} = N_{\text{qp}}/V$ but reaches a maximum value, so that

$$\tau_{\text{qp}}^{-1} = 2Rn_{\text{qp}} + \tau_{\text{max}}^{-1}, \quad (4)$$

where R is the recombination constant. The mechanism by which τ_{qp} saturates is not understood, but it has been suggested that it results from quasiparticle trapping.

The reduction in τ_{qp} with increasing n_{qp} results in an optical response that decreases with increasing power

absorbed by the detector, P_{abs}, as

$$\frac{\delta n_{\text{qp}}}{\delta P_{\text{abs}}} = \frac{\eta_{\text{pb}}\tau_{\text{qp}}}{V\Delta_0} = \frac{\eta_{\text{pb}}\tau_{\text{max}}}{\Delta_0 V}\frac{1}{\sqrt{1 + \eta_{\text{pb}}P_{\text{abs}}/P_*}}, \quad (5)$$

with $P_* = \Delta_0 V/(4\tau_{\text{max}}^2 R)$. Under optical illumination, the photon-shot-noise contribution to the PSD of fractional frequency fluctuations is then $S_{xx} = S_N(\delta x/V\delta n_{\text{qp}})^2$, where the quasiparticle number fluctuation is

$$S_N^\gamma(f) = 2h\nu P_{\text{abs}}\left(\frac{V\delta n_{\text{qp}}}{\delta P_{\text{abs}}}\right)^2$$
$$= \frac{\eta_{\text{pb}}h\nu V}{2\Delta_0 R}\frac{\eta_{\text{pb}}P_{\text{abs}}/P_*}{1 + \eta_{\text{pb}}P_{\text{abs}}/P_*}\frac{1}{1 + (2\pi\tau_{\text{qp}}f)^2}, \quad (6)$$

which has a roll-off determined by τ_{qp}. The wave noise contribution is neglected as the photon occupation number $n_0 \ll 1$. The white noise region of the spectrum approaches a constant value in the limit of high optical power $P \gg P_*$. Pair-breaking detectors incur an additional noise term due to the recombination of quasiparticles. Expressed as a quasiparticle number fluctuation, $S_N^R = 2N_{\text{qp}}\tau_{\text{qp}}/[1 + (2\pi\tau_{\text{qp}}f)^2]$ [48], which approaches V/R in the high optical power limit. The recombination noise is much smaller than the photon noise as $\eta_{\text{pb}}h\nu \gg 2\Delta_0$.
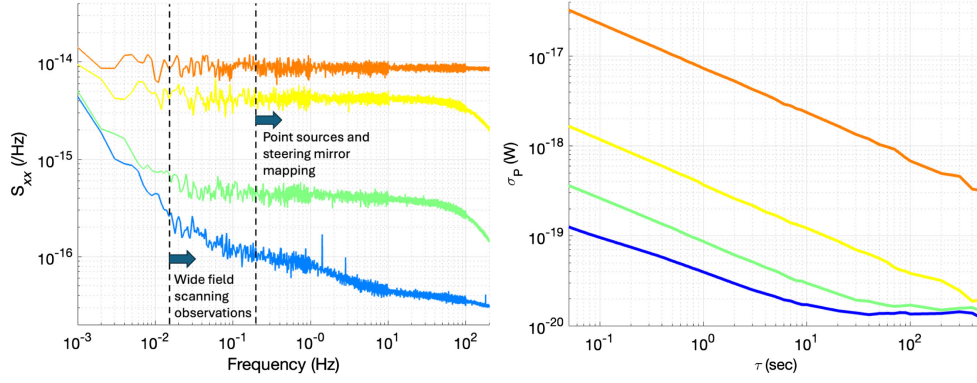
FIG. 6.   Left: fractional frequency noise power spectra for (from bottom to top) $P_{abs} = 0$, 0.6 aW, 11 aW, and 3.5 fW. Right: corresponding Allan deviation plot showing stability out to tens to hundreds of seconds.

D. Quasiparticle conversion efficiency from noise

A second method of deriving η_{pb} compares the measured noise under photon illumination to thermal generation-recombination (GR) noise and provides η_{pb} independently of knowledge of both the precise inductor volume and the quasiparticle response dx/dN_{qp}.

The GR noise is measured by raising the base temperature of the detector. The noise spectra are shown in Appendix C and show a similar behavior to the noise spectra under optical illumination. The low-frequency white noise component of the Lorentzian spectra increases initially with increasing temperature and then saturates when the quasiparticle density becomes high enough that $Rn_{qp} \gg 1/\tau_{max}$. At that point, $S_N^{GR}(0) = 4N_{qp}\tau_{qp} = 2V/R$ [48]. Comparing the measured photon and thermal GR noise saturation values, we find that

$$\frac{S_x^{\gamma}(0) + S_x^R(0)}{S_x^{GR}(0)} = \frac{1}{2}\left(\frac{\eta_{pb}h\nu}{2\Delta_0} + 1\right) = 17.6, \tag{7}$$

which suggests $\eta_{pb} = 0.28$, in rough agreement with the single-photon pulse height analysis presented above. Using this value in Eq. (6) and comparing to the measured photon noise saturation with $\delta x/\delta N_{qp} = 2 \times 10^{-8}$, we find the recombination constant $R = 14.8$ $\mu m^3/s$.

E. Integrating mode dynamic range

From Fig. 5, it can be seen that the detector is near shot noise limited over about 6 orders of magnitude in absorbed power. Because the response $\delta x/\delta P$ of a KID falls off with increasing optical power as $P^{-1/2}$ for $P > P_*$ while the sensitivity required to be photon noise limited is reduced by the same factor, the dynamic range of the detector is potentially quite large. A practical limit to the power that can be absorbed while maintaining shot-noise-limited sensitivity is imposed by the degradation of the quality factor due to quasiparticle loss. The loss per quasiparticle is roughly constant and is related to the

frequency response as

$$\frac{Q_i^{-1}}{N_{qp}} = \frac{2\sigma_1(f_r, T)}{\sigma_2(f_r, T)} \frac{\delta x}{\delta N_{qp}}, \tag{8}$$

where $\sigma(f_r, T) = \sigma_1 - i\sigma_2$ is the complex conductivity. At 600 MHz, $\sigma_1/\sigma_2 \approx 0.15$, several times less than at gigahertz frequencies typically used for KID readout. Hence, the response of the resonator loss is reduced relative to the frequency response for low readout frequencies, enhancing the dynamic range. The lowest Q_i that can be tolerated is primarily determined by the multiplexing factor. For 1000 detectors per readout line and frequencies distributed in the range from 0.4 to 2.4 GHz (see Appendix F), it is reasonable to require $Q_i \gtrsim 10^4$. Using $N_{qp} \approx (V\eta_{pb}P_{abs}/R\Delta)^{1/2}$, we estimate $Q_i \approx 10^4$ with $P_{abs} = 100$ fW, in good agreement with the measurements.

F. Low-frequency stability

We have studied the stability of our devices by obtaining 6-hour datasets with the detector held at 150 mK and the blackbody controlled at fixed temperature. The data are presented both as power spectra and as the Allan deviation in Fig. 6. We find these detectors to be stable to approximately 100 s at < 0.1 aW loading and to > 300 s for loading > 7 aW, corresponding to frequencies of 10 and 3 mHz, respectively. The dependence of the noise knee frequency or corresponding Allan time inflection point on loading is expected, since the white photon noise increasingly overtakes the low-frequency device noise as loading is raised. The results are consistent with an additive frequency noise term that may be from two-level systems.

Modulation frequencies of approximately 0.5 to approximately 175 Hz have been envisioned for most science experiments with mid- and far-IR space missions thus far, in part due to limitations of previous detector systems. Our demonstrated low-frequency performance exceeds these requirements and offers additional opportunities. It both
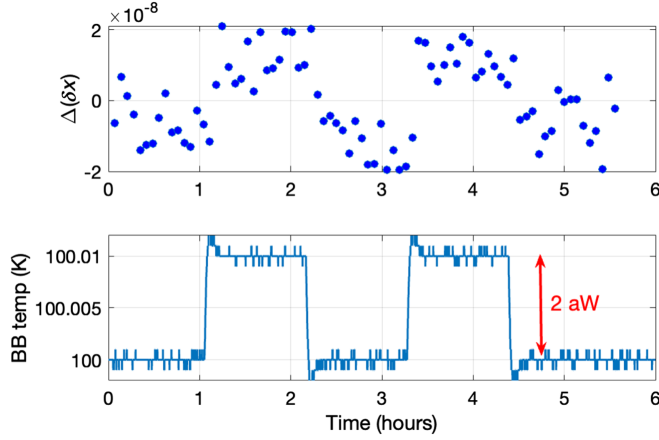
FIG. 7. Time-stream data (top) taken with the blackbody modulated between 100 and 100.01 K with a period of 8000 s. A linear drift term is removed. A 16% transmission neutral density filter is inserted between blackbody and detector for this measurement. The average absorbed power is 3.5 fW, and the modulation is 2 aW. The blackbody thermometer record is shown in the bottom plot.

relaxes requirements on the modulation mechanisms (which are necessarily cryogenic) and enables unique science cases which require long temporal stability. One example is wide-field spectral mapping, also known as line intensity mapping, which requires recovering large-scale (many-degree) modes of the Universe [6]; this necessitates spacecraft scanning which generates modulation frequencies as low as 15 mHz. Another is studying planetary atmospheres as they transit in front of and behind their host stars; these timescales are on the order of hours [2], corresponding to submillihertz frequencies, but typically are accompanied by a large photon noise.

A demonstration of the excellent stability under load is shown in Fig. 7. Here, we show a portion of a time stream taken under a relatively high optical loading of 3.5 fW. The blackbody is modulated by changing its temperature by 10 mK with a period of 8000 s. The points shown are averages over 250 s, and a linear drift of $\delta x/\delta t = 8 \times 10^{-9}$ per hour is removed. The shot noise limit for a 250-s integration time corresponds to $\delta P(\mathrm{rms}) = 4.9 \times 10^{-19}$ W, which is close to the measured noise of 6.6×10^{-19} W, verifying that the noise integrates as expected under optical loading.

IV. METHODS

A. Optical setup

The detector array is mounted to the 50 mK stage of a dilution refrigerator inside a housing designed with the goal of preventing leakage of background thermal photons from higher temperature stages of the cryostat. The cryogenic and optical setup is illustrated in Fig. 8. A set of four metal mesh filters, manufactured at Cardiff
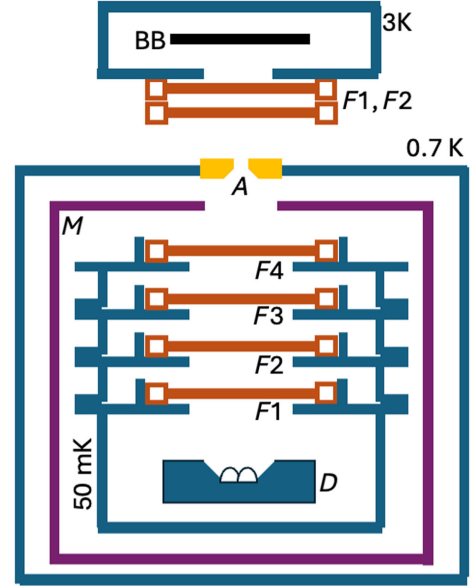

FIG. 8. Diagram of the optical setup. A temperature variable black body (BB) is anchored to the 3 K stage of the dilution refrigerator system and can be heated to approximately 140 K. The microlens-hybridized detector chip (D) is mounted on the 50 mK stage of the refrigerator and is surrounded by a cryoperm magnetic shield (M). It is exposed to the blackbody through a 200-μm-diameter aperture and a set of metal mesh filters: $F1$ (400 cm^{-1} bandpass) and $F2$ (300 cm^{-1} high pass) together form the passband for the blackbody, and $F3$ (600 cm^{-1} low pass) and $F4$ (900 cm^{-1} low pass) provide protection from short-wavelength optical leakage.

University, limit radiation into the detector housing. Two of these filters ($F1$ and $F2$) are bandpass and high-pass filters, which together form a bandpass around $\nu = 12$ THz ($\lambda = 25$ μm). Filters $F3$ and $F4$ are low-pass filters used to block thermal photons that might leak into the system through the pump line. The transmission of all four filters is measured cryogenically in an FTS by the Optics Branch at Goddard Space Flight Center. The detector housing is surrounded by a cryoperm magnetic shield. These structures are located within the 0.7 K thermal shield of the refrigerator, which has been carefully sealed to prevent optical leaks except for a 200-μm-diameter aperture in a 50-μm-thick copper foil through which the detectors view the blackbody.

The blackbody source is a 25-mm-diameter aluminum disk with a surface coated with Aktar Metal Velvet and is located in a separate housing mounted to the 3 K stage of the refrigerator. The emissivity of the Metal Velvet surface is measured at room temperature at Jet Propulsion Laboratory (JPL) and found to be 0.92 within the bandpass of the Cardiff filters. The source is thermally isolated with a Kevlar thread suspension system and can be warmed with a resistive heater to at least 140 K without significantly perturbing the cooling system. An additional set of the $F1$ and $F2$ filters limits the optical band emitted from the
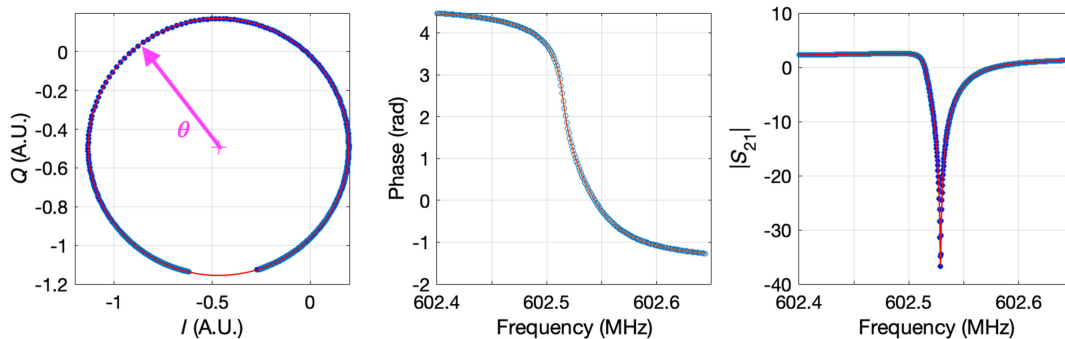
FIG. 9. Left: resonance loop corrected for cable delay. Center: Phase angle around the loop center point versus frequency. Right: Transmission magnitude versus frequency. The red lines in the center and right plots are the fits to the nonlinear resonator model.

blackbody housing. Because of the small size of the aperture compared to a wavelength, it is necessary to include a diffraction correction [42] that characterizes the coupling of the aperture to the blackbody, which we estimate to be 0.9.

B. Measurement of δx

Prior to measuring a particular detector, its resonance curve is determined by sweeping the synthesizer frequency and recording the I and Q outputs of the mixer (Fig. 9, left). The complex data are parametrized in terms of a single phase value θ, representing the angle of the (I, Q) point with respect to the center of the resonance loop. The θ versus frequency curve is fit to a nonlinear resonator model [35,49] (Fig. 9, center and right). The $\theta(f)$ result from the fit is then inverted and used to convert measured I and Q time streams into δx.

C. Measurement of $\delta x / \delta P_{\mathrm{abs}}$

The fractional frequency responsivity as a function of optical power, $R_{\delta x}(P_{\mathrm{abs}}) = \delta x(P_{\mathrm{abs}}) / \delta P_{\mathrm{abs}}$, is determined by imposing a small modulation on the blackbody temperature. The modulation amplitude is chosen to produce an optical power modulation of the greater of either 1 aW or one percent of the average power. Because of the long thermal time constant of the blackbody, the dwell time at each temperature is set at 250 s and a time stream of several hours is collected and averaged over the modulation period,
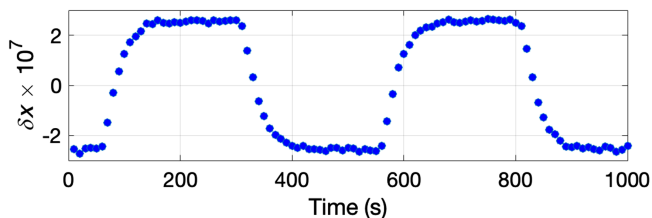

FIG. 10. Average of two periods of the blackbody temperature modulation between 80 and 80.12 K.

as shown in Fig. 10. The frequency shift for each period is determined by differencing the average high- and low-amplitude sections of the modulation. Data during the modulation transition time are ignored. The responsivity is taken as the mean frequency shift over the course of the several-hour modulated time stream.

D. Single-photon data analysis method

A pulse-selection algorithm is used to generate clean samples of single-photon pulses from 50 kHz fractional frequency shift time streams. This is done by (i) applying an order 3 median filter, (ii) convolving with a simple pulse model (falling exponential) to identify temporal locations of potential pulses, (iii) tagging events that stay above an amplitude threshold for a certain number of samples, (iv) removing tagged events above a second, much-higher amplitude threshold (to eliminate cosmic ray events), leaving the remainder as single-photon candidates, and (v) selecting on a rise time criterion characteristic of energy deposition processes. The threshold value is given in multiples of the standard deviation (σ) of the total signal with the blackbody at 30 K. We find 3σ as the optimal threshold for detecting 25 μm photons and rejecting noise spikes. An amplitude cutoff value can be set as an additional selection measure to isolate the noise peak in Fig. 3, where a $\delta x > 0.9 \times 10^{-6}$ cutoff retains 97% of the selected pulses. These successive steps provide time stamps used to pick out photonlike pulses from the raw time streams. The photonlike pulses are then processed with an OF routine [50]. Since the OF evaluates only individual pulses, pulses separated by less than 1.6 ms from a temporal neighbor are discarded. We perform a first-pass causal OF with a simple template to extract pulse onset times and then stack and average pulse events to construct a single-photon template (Fig. 2). This template is then used for a second-pass causal OF. We perform basic data-quality χ^2 and timing cuts to select a batch of clean single-photon events which are studied in detail (Fig. 3).

TABLE I.   The effects of minimal cutoff amplitudes on the DCR and the 30 K photon distribution. The DCR is computed with 8000 s of data, with the blackbody at 3 K. Both the 3 K DCR and 30 K distribution are processed through our 3σ pulse-selection algorithm and corrected for the dead time of the algorithm.

Cutoff amplitude (δx_{cut})	0.9×10^{-6}	1.0×10^{-6}	1.2×10^{-6}
Dark count rate	6.6 mHz	5.3 mHz	4.4 mHz
30 K population above cutoff	97%	94%	80%
30 K detection efficiency	93%	96%	99%

The dark count rate (DCR) is computed by applying the pulse-selection algorithm to time streams collected with the blackbody at 3 K. The algorithm is set to the 30 K 3σ threshold (clean selection of 12 THz photons in the optical measurements, maroon histogram in Fig. 3). Cosmic ray events are excluded from the DCR in two steps. The pulse-selection algorithm automatically separates pulses above a maximum threshold amplitude. To account for cosmic rays that impact the chip far from the studied resonator and, thus, are seen as low-amplitude pulses similar to 25 μm photons, we use a coincidence trigger between the 602 MHz resonator and a neighboring pixel to flag simultaneous events within a 40 μs window.

The DCR for pulselike events with amplitudes $\delta x > 1.2 \times 10^{-6}$ is 4.4 mHz. As this amplitude cutoff is lowered, more pulselike events are captured, leading to an increased DCR. Table I shows some representative values, and we note lower detection efficiencies for lower pulse amplitudes, i.e., when SNR is lower. These efficiencies are computed through data-driven simulations. Noise is simulated from 3 K blackbody time streams with random phase rotations which maintain the measured fractional frequency PSD. A comb of pulses, derived from the OF template with varying amplitudes (a), are added to the synthetic noise. The new noise plus pulse peak amplitudes are binned similarly to the δx distributions in Fig. 3. For each bin, the number of pulses detected by the pulse-selection algorithm N_D and the number of injected pulses N_I is recorded. The detection efficiency above a cutoff amplitude δx_{cut} is calculated as

$$\text{eff}(\delta x_{cut}) = \frac{\sum_{a > \delta x_{cut}} N_D(a) n_{3\sigma}(a) \alpha_{DT}}{\sum_{a > \delta x_{cut}} N_I(a) n_{3\sigma}(a)}, \qquad (9)$$

where $n_{3\sigma}(a)$ is the weight of each bin in the 3σ distribution from Fig. 3 and α_{DT} is the dead time correction.

The dark count rates in Table I reflect monitoring of two detectors simultaneously to allow some removal of coincident events, described in Appendix E. The remaining pulses largely have photonlike rise and decay times and may be from thermal photons leaking into the cryostat through the pump line. The ultimate limits to the DCR will be evaluated in future measurements using a fully dark device housing and a full-array multichannel readout system to allow more reliable simultaneous event detection.

V. DISCUSSION

The measurements that we have presented describe a very versatile detector that is enabling for applications over a wide range of input optical powers. The NEP exceeds that of the best transition-edge-sensed (TES) bolometers demonstrated to date, which have shown NEPs in the 10^{-19} W/Hz$^{1/2}$ range operating at temperatures of 50–100 mK [51–53]. Lower NEPs with TES sensors are a possibility at lower temperatures and/or with exotic isolation (low-thermal-conductance) structures, but device speed becomes a limitation for the most sensitive TESs, which require very low thermal conductance. It is worth noting that, from a practical standpoint, achieving the fundamental sensitivities of TES systems requires exquisite control of stray rf power, while our KIDs and other pair-breaking detectors are essentially immune to rf since they do not respond to photons below the gap energy (approximately 90 GHz for aluminum). Another challenge of TES devices is coupling; light concentration to the absorber is typically required as with our KIDs, but silicon microlenses are not a natural fit because they must be physically isolated from the detectors. Free-space horns have been proposed and prototyped [54,55], but obtaining high performance with horns at the short far-IR wavelengths is difficult.

The excellent sensitivity of our KIDs is important for very low power applications including direct dark-matter detection experiments or space-borne far- to mid-IR spectrometer or interferometer instruments operating near the background limit set by zodiacal dust emission. One leading example is the FIRESS spectrometer [56] on the PRIMA far-IR probe [5], for which these detectors are prototypes. In these low-power applications, the photon arrival rate can be less than 1 per time constant, and, with a suitable readout system, photon counting can provide a means of overcoming electronic noise and the low-frequency TLS device noise. In this mode, the performance metric shifts from noise equivalent power to dark counts or extraneous signals that are not coincident across many detectors simultaneously (coincidences can be identified and removed). Examples might include scattered optical photons, secondary low-energy events from cosmic rays, or background radioactivity. These typically present larger excitation than the photon pulses and so can be discriminated from them and removed.

At higher optical power, corresponding to bright sources, the detector measures the integrated photon energy. In this regime, stability is a key performance goal for many applications. For example, a possible avenue toward detecting exoplanetary life is through mid-IR transit spectroscopy [57,58]. At $\lambda = 25$ μm, the planet to star contrast ratio for an Earth-like planet orbiting an M dwarf star is a few thousand. The hour-scale stability demonstrated in Figs. 6 and 7 would allow relevant spectral lines to be measured over the secondary eclipse. As shown in Appendix B, the detector can easily modified to work in the 5–20 micron range most relevant for mid-IR transit spectroscopy.

The ultimate limit for KIDs in total power mode at low modulation frequencies is TLSs [59] in the capacitive elements of the resonator, which create device-level frequency fluctuations indistinguishable from optical power. The TLS noise contribution is particularly evident below 10 mHz at low optical loading in the noise spectra shown in Fig. 6, where the slope of the noise crosses over to a $1/f$ dependence expected from theory [60]. By measuring the readout power dependence of the quality factor at low readout powers, we determine the intrinsic TLS loss factor $F\delta_0 \approx 10^{-5}$ which points to a significant TLS population, consistent with our measured noise. However, the effect of TLS noise is mitigated in our devices by the high photon response. Additional improvements are possible, as our measured frequency fluctuation noise is actually poorer than observed with larger, less responsive KIDs. A promising avenue is to simply change the capacitor metal to one with better surface quality. Vissers *et al.* [61] show frequency fluctuation variance a factor of 100 lower than our measured value at 1 Hz using titanium nitride capacitors. If paired with our inductor, this improved TLS noise level would produce a factor of 10 further improved sensitivity at low modulation frequencies. Another avenue to reduce the TLS noise is to increase the responsivity further by decreasing the absorber volume at the cost of reduced dynamic range. Calculations of the focused optical spot size suggest that the absorber diameter may be reduced by a factor of 2 with only a few percent efficiency loss, improving the responsivity by a factor of 4.

Our measurements and understanding of the blackbody setup suggest a low coupling efficiency $\eta_o = 0.46$. Based on our validation of the absorber design described in Appendix B and simulations using the measured lenslet profile, this issue does not seem to be fundamental. Optimization of the lenslets and minimization of the thickness of the epoxy bond layer between detector and lenslet array substrates can be expected to yield $\eta_o \gtrsim 0.9$. The addition of a back short located $\lambda/4$ behind the absorber would also improve the detector response, increasing the peak $\mathcal{A}_{\mathrm{abs}}(\nu)$ from approximately 0.7 to close to 1.

VI. CONCLUSION

The detector design presented above extends the state of the art for mid- to far-IR photon detection by providing a solution for detector arrays with thousands to tens of thousands of pixels that simultaneously meet the three cardinal performance requirements of future instruments and experiments. Our devices show (a) zodi-limited sensitivity for moderate-resolution ($R \sim 100$) spectroscopy, including photon counting at low powers, (b) natural dynamic range suitable for virtually any envisioned astronomical measurement, and (c) stability to offer shot-noise-limited performance even on modulation timescales of hours. Further extensions are possible. With lower-noise readout amplifiers [62], the single-photon capability of these detectors should be extensible out to much longer wavelengths, enabling, for example, photon counting with very-high-spectral-resolution (e.g., $R \sim 10^5$) instruments in the 100–200 micron range. The low-frequency stability can be further improved with demonstrated approaches to reduce TLS noise.

APPENDIX A: $\delta x / \delta N_{\mathrm{qp}}$

The response of the fractional frequency δx to changes in the quasiparticle density can be written as

$$\frac{\delta x}{\delta N_{\mathrm{qp}}} = \frac{1}{2}\alpha\gamma_s S_2(f_{\mathrm{res}}, T)\frac{1}{Vn_c}, \qquad (A1)$$

where α is the ratio of the kinetic inductance to the total inductance of the resonator. Based on Sonnet simulations of the inductor geometry and comparison with the experimentally measured resonant frequencies, we find $\alpha = 0.81$. The parameter γ characterizes the scaling of the surface impedance with the complex conductivity $Z_s \sim \sigma^{-\gamma}$. For our 40-nm-thick aluminum film, we estimate a mean free path $l \approx 27$ nm based on a measured sheet resistance $R_{\square} = 0.38\Omega$. The effective penetration depth is

then $\lambda \approx \lambda_L \sqrt{\xi_0/l} = 119$ nm, so the thin film limit applies and $\gamma \approx 1$.

The function $S_2(f_{\mathrm{res}}, T)$ defined in Ref. [63] contains the Mattis-Bardeen equation for σ_2. The value of the function is weakly frequency and power dependent. For $f_{\mathrm{res}} = 600$ MHz and $T = 0.15$ K, $S_2 = 3.96$. The parameter $n_c = 2N_0\Delta$ can be thought of as the density of Cooper pairs.

Using $N_0 = 1.72 \times 10^4/\mu\mathrm{eV}\,\mu\mathrm{m}^3$ for the single spin density of states at the Fermi level and the value of the gap parameter $\Delta = 0.21$ meV determined by fitting the resonator frequency temperature dependence, we find $n_c = 7.3 \times 10^6/\mu\mathrm{m}^3$. Using $V = 11\ \mu\mathrm{m}^3$, we arrive at $\delta x/\delta N_{\mathrm{qp}} = 2 \times 10^{-8}$.

APPENDIX B: RESONANT PHOTON ABSORBER

Techniques for absorbing optical energy in the sensitive inductive element of a KID include the use of antenna structures [64,65] or direct absorption in an area-filling metal structure [66].

For the direct method, the absorber takes the form of a meandering trace and doubles as the inductive element of the resonator. At far-IR wavelengths, the effective surface impedance of the meander should be adjusted to satisfy an impedance matching condition. For example, in the case of illumination through a silicon substrate with refractive index n_{Si} and with a conductive back short located at a distance $\lambda/4$ behind the absorbing surface, the optimal surface impedance is $Z_s = 377/n_{\mathrm{Si}}\Omega$. Without a back short, some power is lost to transmission, and the optimal efficiency is 77% with $Z_s = 377/(1 + n_{\mathrm{Si}})\Omega$.

A parallel array of closely spaced wire traces with sheet resistance R_s, period p, and width w approximates a uniform conducting surface for the polarization with E field parallel to the traces. For $\rho = pn_{\mathrm{Si}}/\lambda \ll 1$, $Z_s \approx pR_s/w$ is real, but Z_s begins to develop a significant imaginary part at $\rho \sim 0.3$ and at $\rho = 1$ power is scattered into grating modes. At short wavelengths, the requirement on ρ implies the need for either a resistive film on the order of $R_s \sim 10$ s of Ohms or very narrow traces. For a silicon substrate and $\lambda = 25\ \mu$m, requiring $\rho < 0.3$ implies a wire period of $p < 2.2\ \mu$m. An efficient absorber could be made using a high-resistivity material like TiN [67]. For example, a 30-nm-thick film with $R_s = 50$ Ohms would need an easily fabricated $w \sim 1\ \mu$m. The resulting absorber volume would be quite large and suitable only for relatively high-background applications.

Use of a more conductive metal film, such as aluminum, results in a low volume by forcing the traces to be much narrower. But for a typical aluminum film sheet resistance of $R_s \sim 1$ Ohm, the needed $w \approx 20$ nm, which would be very challenging to fabricate and may shift the detector operation into a "geiger" or SNSPD mode because of the small superconducting condensation energy per unit length of such a trace.

Another complication with conductive metals is that the surface impedance becomes complex at high frequency where the normal state skin depth becomes comparable to or shorter than the film thickness. For our $t = 40$-nm-thick aluminum film with cold resistivity $1.5\ \mu\Omega \cdot$ cm, the skin depth δ is 18 nm at 12 THz, and the imaginary part of Z_s is comparable to the real part. Because of the imaginary part, an impedance match would be achieved only with the use of a closely spaced (capacitive) back short.

Our solution to impedance matching to aluminum is to make use of resonant structures, similar to what is done in circuit design for matching between unequal or complex impedances. The repeated "hairpin" structure shown in Fig. 1(d) has a resonant response to waves polarized both parallel and perpendicular to the direction of the hairpin, and the details of the geometry can be tuned to adjust the resonance frequencies for the polarizations independently. For example, the length of the hairpin affects mainly the parallel polarization, while the location of the connector that is offset from the end of the hairpin affects mainly the perpendicular polarization resonance.

The absorption efficiency of the structures was simulated in HFSS by considering an infinite array of the repeat structures. The surface impedance of a finite thickness film with conductivity σ is given by Kerr [68]:

$$Z_s = \frac{k}{\sigma} \frac{\exp(kt) + \frac{\sigma Z_\eta - k}{\sigma Z_\eta + k}\exp(-kt)}{\exp(kt) - \frac{\sigma Z_\eta - k}{\sigma Z_\eta + k}\exp(-kt)}, \qquad (\mathrm{B1})$$

where t is the film thickness, $k = (i\omega\sigma\mu_0)^{1/2}$, and $Z_\eta = 377\Omega$ is the terminating impedance on the side of the film opposite the incident wave. When the frequency becomes comparable to the rate of electron scattering events, the conductivity is modified according the Drude formula

$$\sigma(\omega) = \frac{\sigma(0)}{1 + i\omega\tau}, \qquad (\mathrm{B2})$$

where the scattering time $\tau = 13$ fS for our aluminum film. As suggested by Kerr [68], the finite thickness metal film can be modeled as two sheets separated by t with effective surface impedance:

$$Z_x = \frac{1}{2}\left[(2Z_s - i\omega\mu_0 t) + \sqrt{4Z_s^2 + (i\omega\mu_0 t)^2}\right]. \qquad (\mathrm{B3})$$

Results for a range of geometries are shown in Fig. 11. The simulations did not include back shorts, so the maximum expected efficiency is 77%, close to the simulated results. Including a back short, the peak absorption can be increased to greater than 90%. These simulations suggest that this absorber design can be applied over a wide frequency range over the far- and mid-IR bands. Silicon has
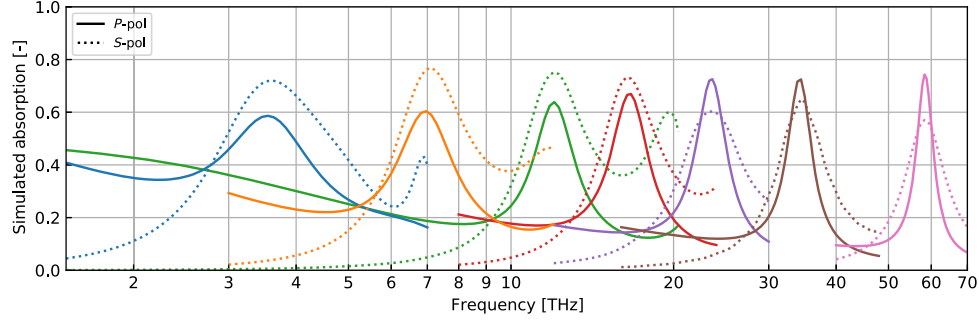
FIG. 11. Simulated absorption efficiency for absorbers designed for 3.5, 7, 12, 24, 34, and 58 THz. The S polarization is in the direction parallel to the hairpin, while the P polarization is along the connected path of the meander structure. The linewidth of the hairpin structure is scaled with frequency from 200 nm at 3.5 THz to 60 nm at 58 THz.

some absorption bands in the mid-IR which could be avoided by switching to a germanium substrate.

In order to experimentally validate the spectral efficiency of the absorber pattern used for the detectors described in the paper, samples are fabricated at JPL with the pattern continuously repeated over a 2 cm by 2 cm area. These samples are cooled to 5 K and measured in transmission in an FTS at NASA Goddard. The raw transmission shown in the upper in Fig. 12 shows Fabry-Perot fringes caused by the cavity of the silicon substrate. The peaks and nulls of the asymmetric Fabry-Perot interferometer (FPI) can be used to determine the absorptance of the patterned mesh [69]. The transmission of an asymmetric FPI (consisting of a silicon cavity with bare silicon on one side and an absorber mesh on the other) can be written as

$$T = \left| \frac{E_t}{E_0} \right|^2 = \left| \frac{t_{\mathrm{Si}} t_{\mathrm{abs}} \exp(i\beta L)}{1 - r_{\mathrm{Si}} r_{\mathrm{abs}} \exp(2i\beta L)} \right|^2, \qquad \text{(B4)}$$

where L is the silicon substrate thickness, $\beta = 2\pi\nu/n_{\mathrm{Si}}c$, and $t_{\mathrm{Si}} = 2/(1 + n_{\mathrm{Si}})$ and $r_{\mathrm{Si}} = (n_{\mathrm{Si}} - 1)/(n_{\mathrm{Si}} + 1)$ are the amplitude transmission and reflection coefficients, respectively, at the silicon surface of the cavity. The mesh absorptance is related to the mesh transmission and reflection coefficients by

$$\mathcal{A}_{\mathrm{abs}}(\nu) = 1 - r_{\mathrm{abs}}(\nu)^2 - t_{\mathrm{abs}}(\nu)^2/n_{\mathrm{Si}}, \qquad \text{(B5)}$$

and we can determine t_{abs} and r_{abs} by evaluating Eq. (B4) at the peaks and nulls of the FPI fringes. The fringe maxima and minima occur when $\exp(i\beta L) = +1$ and -1, respectively, such that

$$T_{\max} = \left| \frac{t_{\mathrm{Si}} t_{\mathrm{abs}}}{1 - r_{\mathrm{Si}} r_{\mathrm{abs}}} \right|^2 \quad \text{and} \quad T_{\min} = \left| \frac{t_{\mathrm{Si}} t_{\mathrm{abs}}}{1 + r_{\mathrm{Si}} r_{\mathrm{abs}}} \right|^2. \qquad \text{(B6)}$$

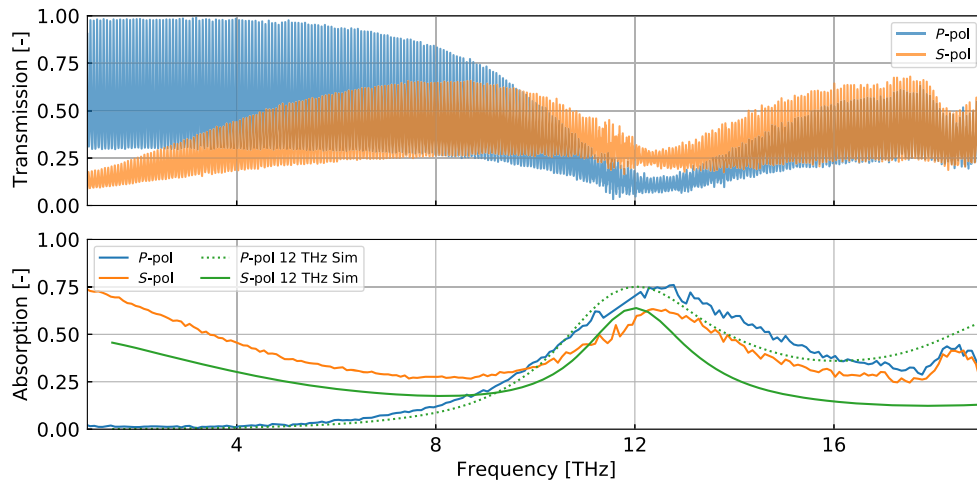Solving the system of equations for t_{abs} and r_{abs} yields

FIG. 12. Top: polarized transmission measurement of the absorber test sample. S pol is parallel to the hairpin, and P pol is orthogonal. Bottom: extracted absorption compared to the simulation result.

$$t_{abs} = \frac{2}{t_{Si}} \left(\frac{1}{\sqrt{T_{max}}} + \frac{1}{\sqrt{T_{min}}} \right)^{-1} \quad \text{and}$$

$$r_{abs} = \frac{1}{r_{Si}} \left(\frac{1 - \sqrt{T_{max}/T_{min}}}{1 + \sqrt{T_{max}/T_{min}}} \right). \tag{B7}$$

By using the peaks and nulls of the data in the upper in Fig. 12 for T_{max} and T_{min} and Eq. (B7), we determine the mesh absorption using Eq. (B5), as plotted in the lower in Fig. 12. The simulated mesh absorption is overplotted on top of the data. We find that the center of the resonance is shifted to slightly higher frequency than designed (12 THz) but that the peak absorption and resonance bandwidth are roughly as expected.

APPENDIX C: BASE TEMPERATURE RESPONSE

A measurement of the resonator frequency versus base temperature is used to determine the superconducting gap parameter Δ_0 by fitting to the Mattis-Bardeen expression for the temperature dependence of the complex conductivity. To avoid fitting simultaneously to both Δ_0 and the kinetic inductance fraction α of the resonator, we first determine α by comparing the measured resonance frequencies to Sonnet simulations of the resonator, varying the aluminum absorber sheet inductance until the simulated resonance frequency matches. Using this procedure, we determine $\alpha = 0.81$.

The fractional frequency shift with temperature is shown in the left in Fig. 13. At low temperatures, the resonance shifts to higher frequency with increasing temperature due to the influence of TLSs at interfaces [70]. Both the dielectric temperature dependence and the low-temperature, low-power dielectric loss are connected to the product of the TLS filling factor and the intrinsic TLS loss tangent $F\delta_0$, which we determine by measuring the resonator internal quality factor Q_i versus excitation power (right in Fig. 13).

The measured Q_i versus power are fit to the TLS loss power dependence [71]

$$Q_{i,\text{TLS}}^{-1} = F\delta_0 \frac{\tanh(hf_{res}/2k_bT)}{\sqrt{1 + P/P_c}} + Q_x^{-1}, \tag{C1}$$

where f_{res} is the resonator frequency, Q_x an additional loss mechanism of undetermined origin, and P_c can be related to a characteristic electric field E_c of the TLS material. The measurement is done at 70 mK, which is the lowest temperature accessible on the stage of the cryostat on which the sample is mounted. The fit yields $1/F\delta_0 = 1.0 \times 10^5$. The resonator Q_i values are higher than that value due to both the temperature dependence and the power dependence in Eq. (C1). That value is then used in the model for the TLS contribution to the temperature-dependent frequency shift [71]:

$$\frac{\delta\epsilon}{\epsilon} = \frac{2F\delta_0}{\pi} \left\{ \text{Re}\left[\Psi\left(\frac{1}{2} - \frac{hf_{res}}{2\pi i k_b T} \right) \right] - \log\left(\frac{hf_{res}}{k_b T} \right) \right\}, \tag{C2}$$

with Ψ is the complex digamma function, which matches the data reasonably well over an interval of the low-temperature range. The $\delta x(T)$ data are then fit to a single parameter Δ yielding 0.21 meV.

The fractional frequency noise for several base temperatures is shown in the left in Fig. 14. The fits to these noise PSDs are used to derive the recombination time of thermally generated quasiparticles shown in the right in Fig. 14. The solid lines in that figure are predictions of the Kaplan theory [72] for two choices of parameters. The red line uses the T_c and gap values for bulk aluminum along with characteristic time $\tau_0 = 438$ ns given by Kaplan. A better fit is found using the measured gap parameter determined above and the corresponding BCS T_c value along with $\tau_0 = 182$ ns. The recombination constant
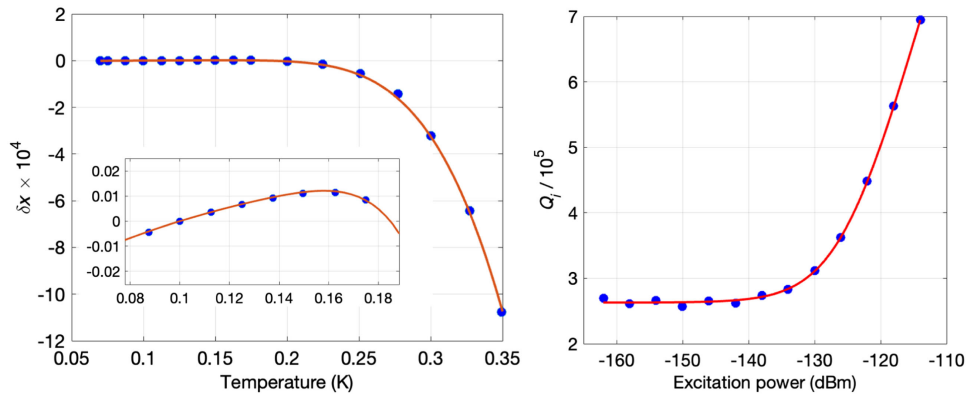

FIG. 13.   Left: fractional frequency shift of the 602 MHz resonator versus base temperature. The red line is a fit to the Mattis-Bardeen temperature dependence including a TLS contribution. Inset: detail of the low-temperature behavior. Right: measured internal quality factors Q_i, derived from fits to vector network analyzer scans of the 602 MHz resonance, as a function of drive power.
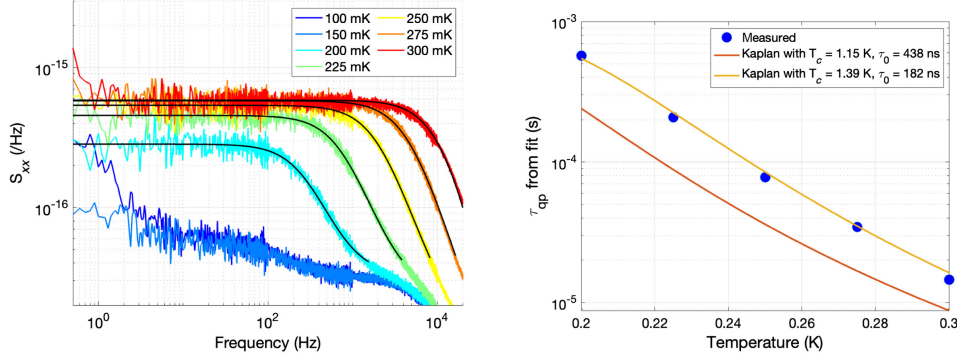
FIG. 14.   Left: fractional frequency noise measured at several base temperatures. The solid lines are fits to a single pole roll-off. Right: quasiparticle lifetimes extracted from noise fits.

$$R = \left(\frac{2\Delta}{k_b T_c}\right)^3 \frac{1}{4 N_0 \Delta \tau_0} = 16.5 \; \frac{\mu m^3}{s}, \qquad \text{(C3)}$$

which is close to the value found in Sec. III D.

APPENDIX D: UNIFORMITY ACROSS THE ARRAY

The upper in Fig. 15 shows the $S21(f)$ transmission through the 44-element KID array. The achieved resonator yield is $41/44$ (93%). Each resonator is fit to a nonlinear resonator model [35,49]. The extracted internal and coupling quality factors (Q_i and Q_c, respectively) are shown in the lower in Fig. 15. The quality factors are all within their designed ranges. The resonator that is studied in depth in the results presented in this manuscript is located at 602 MHz and has very similar properties to the rest of the resonators in the array.

Figure 16 shows the factional frequency noise power spectra for eight different resonators in the array, measured with incident optical power of 0.2 aW. The 602 MHz that is studied in depth in the results presented

above is shown in dark purple. The spectra of all eight resonators show similar properties including white noise level, quasiparticle recombination roll-off, and low-frequency TLS noise ($S_{TLS} \propto f^{1/4}$).

The blackbody coupling is found to be similar across these same eight resonators. The mean photon count rate with the blackbody at 30 K is $5.15 \; s^{-1}$ with a standard deviation of $0.28 \; s^{-1}$, implying the efficiency factor η_o shown in Fig. 4 is uniform across the device.

To further assess uniformity of the responsivity, fractional frequency shifts are determined for all 41 resonators between two blackbody powers (53 zW and 220 fW). The results are plotted in Fig. 17. The eight KIDs without microlenses are clearly separated from the 33 KIDs with microlenses. The lensed KIDs have an average fractional frequency shift of $7\times$ the unlensed KIDs, which corresponds to a detected power ratio of approximately 50. That ratio is smaller than the ratio of the lenslet to the bare absorber area $(870/70)^2 = 150$. The observed photon rate on the unlensed 684 MHz resonator is measured at 40, 42, 44, and 45 K, with corresponding efficiencies for the predicted photon flux Γ_γ [Eq. (2)] found to be
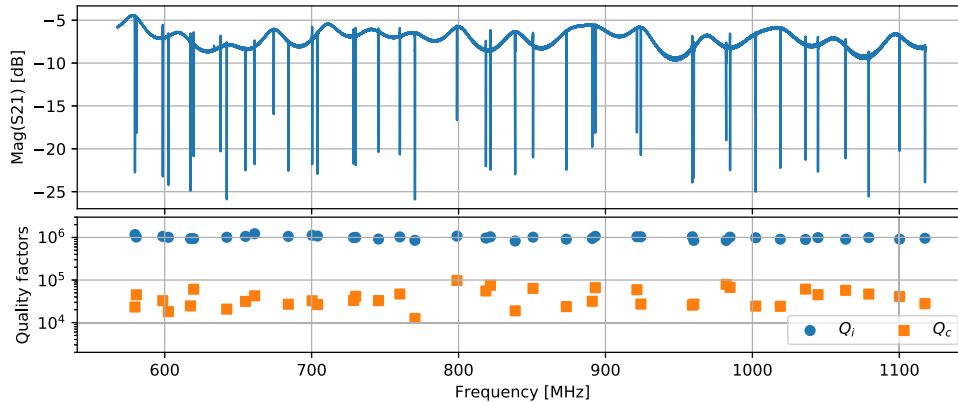

FIG. 15.   Upper: $S21(f)$ measurement of the 44-pixel array shows a yield of 41 resonators between roughly 570 and 1120 MHz. Lower: distribution of internal and coupling quality factors (Q_i and Q_c, respectively) as a function of resonator frequency.
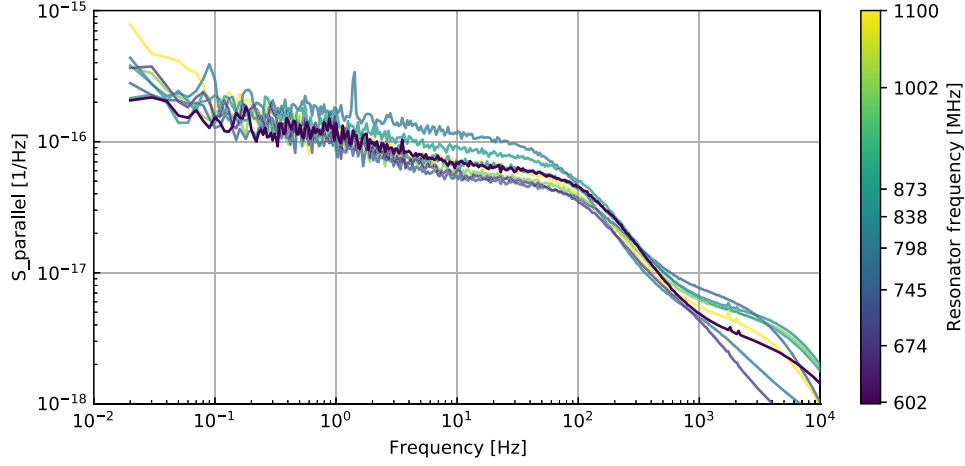
FIG. 16.   Fractional frequency noise spectra of eight optical resonators. The incident power on the microlens of each detector is 0.2 aW.

$\eta_o = 1.04$, 1.00, 1.00, and 0.92, respectively. This suggests that the microlens is acting nonideally, as the predicted flux model describes loading on the bare detectors with η_o near unity. However, the decreasing trend in the dark efficiencies may indicate contributors subdominant to the microlens, such as an aperture thickness effect, scattering from the other metal structures of the pixel, or other stray light reflected within the silicon substrate.

To provide further context, we note that 1008-pixel KID arrays with a different pixel design targeting 210 micron absorption have been produced in the same JPL foundry. The best of these chips show very high resonator yield (>95%) [16]. While sensitivities are not as exquisite as those of the 25-micron chip detailed in this paper, the subset of 292 KIDs which are accessible with the current readout system shows a modest spread in NEP, with 92% below 1×10^{-19} W Hz$^{-1/2}$ at 10 Hz [45].

APPENDIX E: COINCIDENCE TRIGGERING

Two homodyne circuits are combined to collect simultaneous S_{21} measurements of the 602 and 1079 MHz resonators. These resonators are spatially directly adjacent, with a spacing of 900 μm between their absorbers.

A nearest-neighbor pair is chosen to maximize the likelihood of a extraneous event, such as a cosmic ray, exciting both resonators. A 25 μm photon will be seen only as a pulse in a single resonator.

Figure 18 shows the amplitudes of pulselike events detected in either resonator. Blue points indicate events seen in the 602 MHz resonator, with corresponding δx value for the 1079 MHz resonator taken to be the maximum value in a 40 μs window around the time the peak of the pulse seen in the 602 MHz resonator. Red points are similarly defined for the events seen in the 1079 MHz resonator. The point distribution can be divided into a low-amplitude noise ball, a central region of shared pulses belonging to cosmic ray events, a horizontal lobe for photon pulses in the 602 MHz resonator, and a vertical lobe for photon pulses in the 1079 MHz resonator.
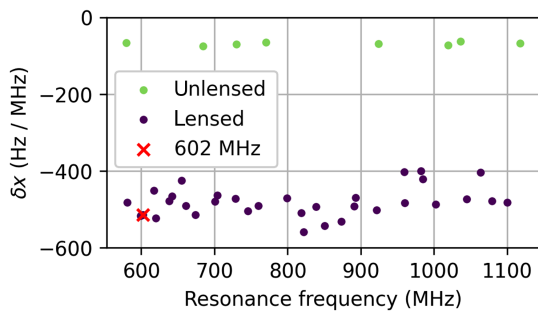

FIG. 17.   Fractional frequency shift versus resonance frequency for 41 KIDs. The incident power on each detector is 220 fW. The 602 MHz KID under study in this paper is plotted as a red X.

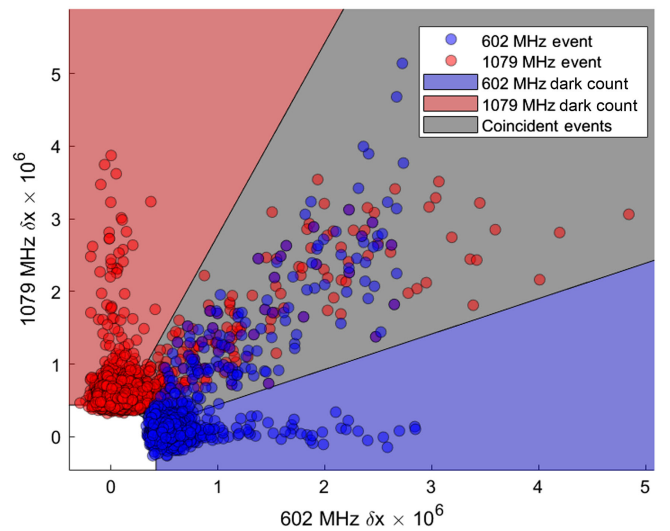FIG. 18.   Simultaneous measurements of the factional frequency shift for the 602 and 1079 MHz resonators over 8000 s of data.

The shared event region is defined by extending 3 standard deviations above and below the best fit line to the central data outside the noise ball. Setting a cutoff amplitude and counting pulses in the horizontal lobe gives the DCR in Table I.

APPENDIX F: MULTIPLEXING

Digital readout multiplexing electronics suitable for the detectors described in this paper have been developed by several groups [28,73,74]. The noise contributed by these systems is limited by the SNR of the analog-to-digital converter and increases with the number of multiplexed detectors, because the dynamic range of the analog-to-digital converter must be shared by all of the readout tones. Van Rantwijk *et al.* [28] measured a phase noise $S_\theta = -96$ dBc/Hz for 1000 tones. With $Q = 20000$, the contribution of the multiplexer to the fractional frequency noise is then

$$S_{xx} = 10^{S_\theta[\text{dB}]/10}/4Q^2 = 1.6 \times 10^{-19}/\text{Hz}, \quad \text{(F1)}$$

which is well below the measured noise shown in Fig. 5.

So, despite their exceptional sensitivity, our detectors place relatively weak demands on multiplexer performance. In part, this is due to their high responsivity that results from very small inductor volume and long quasiparticle lifetime. The kinetic inductance fraction α is also high relative to other FIR KID designs, further enhancing the responsivity.

Another aspect of the detector design that enhances multiplexing is the low resonator frequency range. The large absorber inductance allows for resonance frequencies as low as 400 MHz with the same IDC capacitor linewidth and spacing as used in this work. For the 1000-pixel arrays in development, the target frequency range of 0.4–2.4 GHz fits in the 2 GHz bandwidth of demonstrated multiplexer implementations but covers a large fractional bandwidth of 2.6 octaves. For fixed Q, larger fractional bandwidth results in higher dynamic range, as a larger fractional frequency shift can be accommodated before causing a collision with another resonator, and also lower frequency collision probability due to random process variations.

APPENDIX G: OPERATION IN THE SPACE ENVIRONMENT

Many of the most exciting scientific applications of the KIDs are from space-borne observatories, so it is important to consider short- and long-term effects on their operation due to the ionizing particle environment of space. On short timescales, energy deposited by cosmic ray interactions will be observed in the detector time streams. On longer timescales, one may ask if the detectors degrade in some fashion as a result of cosmic ray interactions over the course of a several-year mission. For example, with photoconductive detectors, cumulative displacement damage can increase dark current.

The time-stream effect in KIDs has been studied by our group [75] and the SRON KID group [76]. High-energy particles including protons, heavy ions, muons, and gamma rays deposit energy in the silicon substrate as they pass through. In a given event, the energy manifests as athermal phonons which traverse the silicon substrate and arrive at a KID inductor to break Cooper pairs and thereby create a glitch with a fast rise followed by decay with timescale given by the quasiparticle lifetime (approximately 1 ms in sensitive KIDs). The per-pixel rate depends on the flux of particles and the effective area on the substrate over which the athermal phonons from a given particle propagate to impact KIDs. The key to mitigation, demonstrated by both groups, is to reduce this effective area by including an additional metal layer to absorb the phonons. This is an area of active study, but the initial prognosis is good. Using the well-known proton fluxes at Earth-Sun L2 from the Planck experiment [77], combined with lab measurements of the glitch rate due to natural radioactivity in terrestrial labs, Kane *et al.* [75] predict an effective dead time in flight of only 2% due to cosmic rays in our KID arrays. Further study is under way as the array design for flight is matured.

While the time-stream glitches are an important area of study and optimization, the total dose effects are not an important consideration, because the thin superconducting films used in KIDs are not susceptible to displacement damage. An upper limit to the total integrated effect that may produce impurities or nuclear dislocations is given by the displacement damage dose (DDD); for example, a conservative benchmark is 2.6×10^8 MeV/g for a 5-year mission at Earth-Sun L2. This total DDD corresponds to an estimated fraction of impacted nuclei of four parts per billion (ppb), given a 3-eV typical displacement energy. This tiny fraction is negligible compared to material purity (1000–10 000 ppb) and natural grain boundaries to which our KIDs may be sensitive. Experiments with aluminum KIDs have borne out this basic immunity, with both proton bombardment exceeding the fiducial 5-year dose [78] and ion implantation ranging up to 5000 ppb, before which there was no degradation [79]. This is in contrast with some semiconducting devices which can suffer degradation at impurity levels as low as 0.1 ppb.

---

[1] A. Dyrek, E. Ducrot, P.-O. Lagage, P. Tremblin, S. Kendrew, J. Bouwman, and R. Bouffet, *Transiting exoplanets with the mid-infrared instrument on board JWST: From simulations to observations*, Astron. Astrophys. **683**, A212 (2024).

[2] J. Bouwman *et al.*, *Spectroscopic time series performance of the mid-infrared instrument on the JWST*, Publ. Astron. Soc. Pac. **135**, 038002 (2023).

[3] S. P. Quanz *et al.*, *Atmospheric characterization of terrestrial exoplanets in the mid-infrared: Biosignatures, habitability, and diversity*, Exp. Astron. **54**, 1197 (2022).

[4] C. M. Bradford, B. A. Cameron, B. D. Moore, S. Hailey-Dunsheath, E. G. Amatucci, D. C. Bradley, J. A. Corsetti, D. T. Leisawitz, M. J. DiPirro, J. G. Tuttle, A.-D. Brown, R. McBirney, A. Pope, L. Armus, M. Meixner, and K. Pontoppidan, *Origins Survey Spectrometer: Revealing the hearts of distant galaxies and forming planetary systems with far-IR spectroscopy*, J. Astron. Telesc. Instrum. Syst. **7**, 011017 (2021).

[5] J. Glenn and M. Meixner, *PRIMA: The probe far-infrared mission for astrophysics*, in *American Astronomical Society Meeting Abstracts* (American Astronomical Society, Washington, DC, 2024), Vol. 56, pp. 450–02.

[6] K. S. Karkare, A. Moradinezhad Dizgah, G. K. Keating, P. Breysse, and D. T. Chung, *Snowmass 2021 Cosmic Frontier White Paper: Cosmology with millimeter-wave line intensity mapping*, arXiv:2203.07258.

[7] Y. Gong, A. Cooray, M. Silva, M. G. Santos, J. Bock, C. M. Bradford, and M. Zemcov, *Intensity mapping of the [cii] fine structure line during the epoch of reionization*, Astrophys. J. **745**, 49 (2011).

[8] G. Sun *et al.*, *Probing cosmic reionization and molecular gas growth with TIME*, Astrophys. J. **915**, 33 (2021).

[9] I. Sakon *et al.*, *Mid-infrared spectrometer and camera for the Origins Space Telescope*, J. Astron. Telesc. Instrum. Syst. **7**, 011013 (2021).

[10] P. K. Day, H. G. LeDuc, B. A. Mazin, A. Vayonakis, and J. Zmuidzinas, *A broadband superconducting detector suitable for use in large arrays*, Nature (London) **425**, 817 (2003).

[11] J. J. A. Baselmans, J. Bueno, S. J. C. Yates, O. Yurduseven, N. Llombart, K. Karatsu, A. M. Baryshev, L. Ferrari, A. Endo, D. J. Thoen, P. J. de Visser, R. M. J. Janssen, V. Murugesan, E. F. C. Driessen, G. Coiffard, J. Martin-Pintado, P. Hargrave, and M. Griffin, *A kilo-pixel imaging system for future space based far-infrared observatories using microwave kinetic inductance detectors*, Astron. Astrophys. **601**, A89 (2017).

[12] T. Peacock, P. Verhoeve, N. Rando, M. Perryman, B. Taylor, and P. Jakobsen, *Superconducting tunnel junctions as detectors for ultraviolet, optical, and near infrared astronomy*, Astron. Astrophys. Suppl. Ser. **123**, 581 (1997).

[13] P. M. Echternach, B. J. Pepper, T. Reck, and C. M. Bradford, *Single photon detection of 1.5 THz radiation with the quantum capacitance detector*, Nat. Astron. **2**, 90 (2018).

[14] J. J. A. Baselmans, F. Facchin, A. Pascual Laguna, J. Bueno, D. J. Thoen, V. Murugesan, N. Llombart, and P. J. de Visser, *Ultra-sensitive THz microwave kinetic inductance detectors for future space telescopes*, Astron. Astrophys. **665**, A17 (2022).

[15] S. Hailey-Dunsheath, S. Berkel, A. E. Beyer, L. Foote, R. M. J. Janssen, H. G. LeDuc, P. M. Echternach, and C. M. Bradford, *Characterization of a far-infrared kinetic inductance detector prototype for PRIMA*, arXiv:2311.03586.

[16] L. Foote, C. Albert, J. Baselmans, A. D. Beyer, N. F. Cothard, P. K. Day, S. Hailey-Dunsheath, P. M. Echternach, R. M. J. Janssen, E. Kane, H. Leduc, L.-J. Liu, H. Nguyen, J. Perido, J. Glenn, J. Zmuidzinas, and C. M. Bradford, *High-sensitivity kinetic inductance detector arrays for the probe far-infrared mission for astrophysics*, J. Low Temp. Phys. **214**, 219 (2024).

[17] B. Mazin *et al.*, *Optical and near-IR microwave kinetic inductance detectors (MKIDs) in the 2020s*, Bull. AAS **51** (2019), https://baas.aas.org/pub/2020n7i017.

[18] J. Sayers *et al.*, *The status of MUSIC: The multiwavelength sub-millimeter inductance camera*, in *Millimeter, Sub-millimeter, and Far-Infrared Detectors and Instrumentation for Astronomy VII*, edited by W. S. Holland and J. Zmuidzinas, SPIE Conf. Ser. Vol. 9153 (2014), p. 915304, 10.1117/12.2055444.

[19] L. Bing *et al.*, *NIKA2 Cosmological Legacy Survey. Survey description and galaxy number counts*, Astron. Astrophys. **677**, A66 (2023).

[20] M. Calvo *et al.*, *The NIKA2 instrument, a dual-band kilopixel KID array for millimetric astronomy*, J. Low Temp. Phys. **184**, 816 (2016).

[21] A. Ritacco *et al.*, *Polarimetry at millimeter wavelengths with the NIKA camera: Calibration and performance*, Astron. Astrophys. **599**, A34 (2017).

[22] A. Endo *et al.*, *First light demonstration of the integrated superconducting spectrometer*, Nat. Astron. **3**, 989 (2019).

[23] G. Presta, P. Ade, E. Battistelli, M. Castellano, I. Colantoni, F. Columbro, A. Coppolecchia, G. D'Alessandro, P. Bernardis, S. Gordon *et al.*, *The first flight of the OLIMPO experiment: Instrument performance*, J. Phys. Conf. Ser. **1548**, 012018 (2020).

[24] I. Lowe *et al.*, *Characterization, deployment, and in-flight performance of the BLAST-TNG cryogenic receiver*, in *Millimeter, Submillimeter, and Far-Infrared Detectors and Instrumentation for Astronomy X*, edited by J. Zmuidzinas and J.-R. Gao, SPIE Conf. Ser. Vol. 11453 (2020), p. 1145304, 10.1117/12.2560854.

[25] S. R. Meeker *et al.*, *DARKNESS: A microwave kinetic inductance detector integral field spectrograph for high-contrast astronomy*, Publ. Astron. Soc. Pac. **130**, 065001 (2018).

[26] B. A. Mazin, S. R. Meeker, M. J. Strader, P. Szypryt, D. Marsden, J. C. van Eyken, G. E. Duggan, A. B. Walter, G. Ulbricht, M. Johnson, B. Bumble, K. O'Brien, and C. Stoughton, *ARCONS: A 2024 pixel optical through near-IR cryogenic imaging spectrophotometer*, Publ. Astron. Soc. Pac. **125**, 1348 (2013).

[27] O. Bourrion, A. Benoit, J. L. Bouly, J. Bouvier, G. Bosson, M. Calvo, A. Catalano, J. Goupy, C. Li, J.F. Macías-Pérez, A. Monfardini, D. Tourres, N. Ponchant, and C. Vescovi, *NIKEL_AMC: Readout electronics for the NIKA2 experiment*, J. Instrum. **11**, P11001 (2016).

[28] J. van Rantwijk, M. Grim, D. van Loon, S. Yates, A. Baryshev, and J. Baselmans, *Multiplexed readout for 1000-pixel arrays of microwave kinetic inductance detectors*, IEEE Trans. Microwave Theory Tech. **64**, 1876 (2016).

[29] S. Gordon, B. Dober, A. Sinclair, S. Rowe, S. Bryan, P. Mauskopf, J. Austermann, M. Devlin, S. Dicker, J. Gao, G. C. Hilton, J. Hubmayr, G. Jones, J. Klein, N. P. Lourie, C. McKenney, F. Nati, J. D. Soler, M. Strader, and M. Vissers, *An open source, FPGA-based LeKID readout for BLAST-TNG: Pre-flight results*, J. Astron. Instrum. **05**, 1641003 (2016).

[30] A. K. Sinclair, R. C. Stephenson, C. A. Roberson, E. L. Weeks, J. Burgoyne, A. I. Huber, P. M. Mauskopf, S. C. Chapman, J. E. Austermann, S. K. Choi *et al.*, *Ccat-prime: Rfsoc based readout for frequency multiplexed kinetic inductance detectors*, in *Millimeter, Submillimeter, and Far-Infrared Detectors and Instrumentation for Astronomy XI* (SPIE, Bellingham, WA, 2022), Vol. 12190, pp. 444–463.

[31] S. Hailey-Dunsheath, A. C. M. Barlis, J. E. Aguirre, C. M. Bradford, J. G. Redford, T. S. Billings, H. G. LeDuc, C. M. McKenney, and M. I. Hollister, *Development of aluminum LeKIDs for balloon-borne far-IR spectroscopy*, J. Low Temp. Phys. **193,** 968 (2018).

[32] N. F. Cothard, C. Albert, A. D. Beyer, C. M. Bradford, P. Echternach, B. H. Eom, L. Foote, M. Foote, S. Hailey-Dunsheath, R. M. J. Janssen, E. Kane, H. LeDuc, J. Perido, J. Glenn, and P. K. Day, *Parallel plate capacitor aluminum KIDs for future far-infrared space-based observatories*, J. Low Temp. Phys. **214,** 200 (2024).

[33] R. Nie *et al.*, *Absorber design and optimization of kinetic inductance detectors for the terahertz intensity mapper*, J. Low Temp. Phys. **209,** 525 (2022).

[34] N. F. Cothard, T. Stevenson, J. Mateo, N. Costen, K. Denis, J. Perido, I. Schrock, F. Wang, and J. Glenn, *Monolithic silicon microlens arrays for far-infrared astrophysics*, Appl. Opt. **63,** 1481 (2024).

[35] L. Swenson, P. Day, B. Eom, H. Leduc, N. Llombart, C. McKenney, O. Noroozian, and J. Zmuidzinas, *Operation of a titanium nitride superconducting microresonator detector in the nonlinear regime*, J. Appl. Phys. **113,** 104501 (2013).

[36] B. S. Karasik, A. V. Sergeev, and D. E. Prober, *Nanobolometers for THz photon detection*, IEEE Trans. Terahertz Sci. Technol. **1,** 97 (2011).

[37] M. Kurakado, *Possibility of high resolution detectors using superconducting tunnel junctions*, Nucl. Instrum. Methods Phys. Res. **196,** 275 (1982).

[38] A. Kozorezov, J. Wigmore, D. Martin, P. Verhoeve, and A. Peacock, *Electron energy down-conversion in thin superconducting films.*, Phys. Rev. B **75,** 094513 (2007).

[39] P. J. De Visser, S. A. De Rooij, V. Murugesan, D. J. Thoen, and J. J. Baselmans, *Phonon-trapping-enhanced energy resolution in superconducting single-photon detectors*, Phys. Rev. Appl. **16,** 034051 (2021).

[40] N. Zobrist, W. H. Clay, G. Coiffard, M. Daal, N. Swimmer, P. Day, and B. A. Mazin, *Membraneless phonon trapping and resolution enhancement in optical microwave kinetic inductance detectors*, Phys. Rev. Lett. **129,** 017701 (2022).

[41] A. Kozorezov, J. Wigmore, D. Martin, P. Verhoeve, and A. Peacock, *Phonon noise in thin metal films in an advanced energy down-conversion stage*, J. Low Temp. Phys. **151,** 51 (2008).

[42] W. Blevin, *Diffraction losses in radiometry and photometry*, Metrologia **6,** 39 (1970).

[43] A. Kozorezov, A. Volkov, J. Wigmore, A. Peacock, A. Poelaert, and R. Den Hartog, *Quasiparticle-phonon downconversion in nonequilibrium superconductors*, Phys. Rev. B **61,** 11807 (2000).

[44] R. M. J. Janssen, R. Nie, B. Bumble, L.-J. Liu, J. Redford, J. P. Filippini, C. M. Bradford, S. Hailey-Dunsheath, J. E. Aguirre, J. S. Bracks, A. J. Corso, J. Fu, C. E. Groppi, J. Hoh, R. P. Keenan, I. N. Lowe, D. P. Marrone, P. D. Mauskopf, I. Trumper, and J. D. Vieira, *Single pixel performance of the kinetic inductance detectors for the terahertz intensity mapper*, J. Low Temp. Phys. **211,** 197 (2023).

[45] E. Kane, C. Albert, J. Baselmans, R. Basu Thakur, C. Bradford, N. Cothard, P. Day, L. Foote, S. Hailey-Dunsheath, R. Janssen, H. LeDuc, L.-J. Liu, H. Nguyen, and J. Zmuidzinas, *Modeling of cosmic rays and near-IR photons in aluminum KIDs*, J. Low Temp. Phys. **214,** 238 (2024).

[46] T. Guruswamy, D. Goldie, and S. Withington, *Quasiparticle generation efficiency in superconducting thin films*, Supercond. Sci. Technol. **27,** 055012 (2014).

[47] P. J. Visser, J. Baselmans, J. Bueno, N. Llombart, and T. Klapwijk, *Fluctuations in the electron system of a superconductor exposed to a photon flux*, Nat. Commun. **5,** 3130 (2014).

[48] C. Wilson and D. Prober, *Quasiparticle number fluctuations in superconductors*, Phys. Rev. B **69,** 094524 (2004).

[49] X. Dai, X. Liu, Q. He, Y. Chen, Z. Mai, Z. Shi, W. Guo, Y. Wang, L. Wei, M. Vissers *et al.*, *New method for fitting complex resonance curve to study nonlinear superconducting resonators*, Supercond. Sci. Technol. **36,** 015003 (2022).

[50] R. Basu Thakur, *The cryogenic dark matter search low ionization-threshold experiment*, Ph.D. thesis, University of Illinois at Urbana-Champaign, 2015, https://www.proquest.com/docview/1750577891/abstract/88524DBB460E4DAEPQ/1.

[51] A. D. Beyer, P. M. Echternach, M. E. Kenyon, M. C. Runyan, B. Bumble, C. M. Bradford, J. J. Bock, and W. A. Holmes, *Effect of* Mo/Cu *superconducting bilayer geometry on ultra-sensitive transition-edge sensor performance*, IEEE Trans. Appl. Supercond. **23,** 2100104 (2013).

[52] T. Suzuki, P. Khosropanah, M. L. Ridder, R. A. Hijmering, J. R. Gao, H. Akamatsu, L. Gottardi, J. Kuur, and B. D. Jackson, *Development of ultra-low-noise TES bolometer arrays*, J. Low Temp. Phys. **184,** 52 (2016).

[53] E. A. Williams, S. Withington, D. J. Goldie, C. N. Thomas, P. A. Ade, and R. Sudiwala, *Characterizing the optical response of ultra-low-noise far-infrared* 60–110 μm *transition edge sensors*, Rev. Sci. Instrum. **91,** 123104 (2020).

[54] M. D. Audley, G. De Lange, J.-R. Gao, P. Khosropanah, R. Hijmering, M. Ridder, P. D. Mauskopf, D. Morozov, N. A. Trappe, and S. Doherty, *Optical performance of an ultra-sensitive horn-coupled transition-edge-sensor bolometer with hemispherical backshort in the far infrared*, Rev. Sci. Instrum. **87,** 043103 (2016).

[55] E. Williams, S. Withington, D. Goldie, C. Thomas, J. Chen, P. Ade, R. Sudiwala, I. Walker, and N. Trappe, *Ultra-low-noise transition edge sensors for far infrared wavelengths: Optical design, measurement and stray light control*, in *Millimeter, Submillimeter, and Far-Infrared Detectors and Instrumentation for Astronomy IX* (SPIE, Bellingham, WA, 2018), Vol. 10708, pp. 396–408.

[56] C. Bradford *et al.*, *Firess: Unlocking sensitive far-IR spectroscopy with PRIMA*, Bull. AAS **56** (2024), https://baas.aas.org/pub/2024n2i457p11.

[57] J. Staguhn, D. Fixsen, K. Stevenson, S. H. Moseley, E. Sharp, A. D. Brown, J. Fortney, G. C. Hilton, T. Kataria, and E. J. Wollack, *An ultra-stable mid-infrared sensor for the detection of bio-signatures by means of transit spectroscopy*, in *Proceedings of the 2019 IEEE Aerospace Conference* (IEEE, New York, 2019), pp. 1–10.

[58] A. M. Mandell, J. Lustig-Yaeger, K. B. Stevenson, and J. Staguhn, *Mirecle: Science yield for a mid-infrared explorer-class mission to study nontransiting rocky planets orbiting the nearest m stars using planetary infrared excess*, Astron. J. **164**, 176 (2022).

[59] J. Gao, J. Zmuidzinas, B. A. Mazin, H. G. LeDuc, and P. K. Day, *Noise properties of superconducting coplanar waveguide microwave resonators*, Appl. Phys. Lett. **90**, 102507 (2007).

[60] L. Faoro and L. B. Ioffe, *Interacting tunneling model for two-level systems in amorphous materials and its predictions for their dephasing and noise in superconducting microresonators*, Phys. Rev. B **91**, 014201 (2015).

[61] M. R. Vissers, J. E. Austermann, M. Malnou, C. M. McKenney, B. Dober, J. Hubmayr, G. C. Hilton, J. N. Ullom, and J. Gao, *Ultrastable millimeter-wave kinetic inductance detectors*, Appl. Phys. Lett. **116**, 032601 (2020).

[62] N. Zobrist, B.H. Eom, P. Day, B.A. Mazin, S.R. Meeker, B. Bumble, H.G. LeDuc, G. Coiffard, P. Szypryt, N. Fruitwala *et al.*, *Wide-band parametric amplifier readout and resolution of optical microwave kinetic inductance detectors*, Appl. Phys. Lett. **115**, 042601 (2019).

[63] J. Zmuidzinas, *Superconducting microresonators: Physics and applications*, Annu. Rev. Condens. Matter Phys. **3**, 169 (2012).

[64] P. Day, H. Leduc, A. Goldin, T. Vayonakis, B. Mazin, S. Kumar, J. Gao, and J. Zmuidzinas, *Antenna-coupled microwave kinetic inductance detectors*, Nucl. Instrum. Methods Phys. Res., Sect. A **559**, 561 (2006).

[65] A. Baryshev, J. J. Baselmans, A. Freni, G. Gerini, H. Hoevers, A. Iacono, and A. Neto, *Progress in antenna coupled kinetic inductance detectors*, IEEE Trans. Terahertz Sci. Technol. **1**, 112 (2011).

[66] S. Doyle, P. Mauskopf, J. Naylon, A. Porch, and C. Duncombe, *Lumped element kinetic inductance detectors*, J. Low Temp. Phys. **151**, 530 (2008).

[67] J. Perido, P. K. Day, A. D. Beyer, N. F. Cothard, S. Hailey-Dunsheath, H. G. Leduc, B. H. Eom, and J. Glenn, *Parallel-plate capacitor titanium nitride kinetic inductance detectors for infrared astronomy*, arXiv:2312.17378.

[68] A. Kerr, *Surface impedance of superconductors and normal conductors in EM simulators*, MMA Memo No. 245—NRAO Electronics Division Internal Report No. 302 (1999).

[69] J. Perido, *Kinetic inductance detectors and metal-mesh filters for far-infrared astronomy*, Ph.D. thesis, University of Colorado Boulder, 2023, available at https://scholar.colorado.edu/concern/graduate_thesis_or_dissertations/6108vc769.

[70] A. C. Anderson, B. Golding, J. Graebner, S. Hunklinger, J. Jäckle, W. Phillips, R. Pohl, M. Schickfus, and D. Weaire, *Amorphous Solids: Low-Temperature Properties* (Springer, New York, 2012), Vol. 24.

[71] S. Hunklinger and W. Arnold, *Ultrasonic properties of glasses at low temperatures*, in *Physical Acoustics* (Academic Press, 1976), Vol. 12, pp. 155–215.

[72] S. B. Kaplan, C. Chi, D. Langenberg, J.-J. Chang, S. Jafarey, and D. Scalapino, *Quasiparticle and phonon lifetimes in superconductors*, Phys. Rev. B **14**, 4854 (1976).

[73] S. McHugh, B. A. Mazin, B. Serfass, S. Meeker, K. O'Brien, R. Duan, R. Raffanti, and D. Werthimer, *A readout for large arrays of microwave kinetic inductance detectors*, Rev. Sci. Instrum. **83**, 044702 (2012).

[74] R. Duan and S. Golwala, *Readout for kinetic-inductance-detector-based submillimeter radio astronomy*, in *Millimeter, Submillimeter, and Far-Infrared Detectors and Instrumentation for Astronomy X* (SPIE, Bellingham, WA, 2020), Vol. 11453, pp. 252–285.

[75] E. Kane, C. Albert, J. Baselmans, R. Basu Thakur, C. Bradford, N. Cothard, P. Day, L. Foote, S. Hailey-Dunsheath, R. Janssen, H. LeDuc, L.-J. Liu, H. Nguyen, and J. Zmuidzinas, *Modeling of cosmic rays and near-IR photons in aluminum KIDs*, J. Low Temp. Phys. **214**, 238 (2024).

[76] K. Karatsu, A. Endo, J. Bueno, P. De Visser, R. Barends, D. Thoen, V. Murugesan, N. Tomita, and J. Baselmans, *Mitigation of cosmic ray effect on microwave kinetic inductance detector arrays*, Appl. Phys. Lett. **114**, 032601 (2019).

[77] A. Catalano, P. Ade, Y. Atik, A. Benoit, E. Bréele, J. Bock, P. Camus, M. Chabot, M. Charra, B. Crill *et al.*, *Impact of particles on the Planck HFI detectors: Ground-based measurements and physical interpretation*, Astron. Astrophys. **569**, A88 (2014).

[78] K. Karatsu, A. Dominjon, T. Fujino, T. Funaki, M. Hazumi, F. Irie, H. Ishino, Y. Kida, T. Matsumura, K. Mizukami, M. Naruse, T. Nitta, T. Noguchi, N. Oka, S. Sekiguchi, Y. Sekimoto, M. Sekine, S. Shu, Y. Yamada, and T. Yamashita, *Radiation tolerance of aluminum microwave kinetic inductance detector*, J. Low Temp. Phys. **184**, 540 (2016).

[79] R. Barends, S. Van Vliet, J. Baselmans, S. Yates, J. Gao, and T. Klapwijk, *Enhancement of quasiparticle recombination in* Ta *and* Al *superconductors by implantation of magnetic and nonmagnetic atoms*, Phys. Rev. B **79**, 020509 (2009).